



University of Crete

Material Science Department

# High temperature spin polarization in trapped polariton condensates

John Balas

Thesis Committee:

Pavlos Savvidis, Professor (supervisor)

Nikos Pelekanos, Professor

George Deligeorgis, Associated researcher

Heraklion, September 2019

# Table of contents

## 1 Introduction

## 2 Basic theory

### 2.1 Introduction

### 2.2 Matter

#### 2.2.1 Excitons

##### 2.2.1.1 Exciton energy

##### 2.2.1.2 Oscillator strength

##### 2.2.1.3 Quantum wells

### 2.3 Light

#### 2.3.1 DBRs

#### 2.3.2 Planar microcavities with DBRs

### 2.4 Light matter coupling

#### 2.4.1 Quantum description of light

#### 2.4.2 Exciton -photon coupling

### 2.5 Polaritons

#### 2.5.1 Bose-Einstein and polariton condensation

#### 2.5.2 Polariton lasing

#### 2.5.3 Blueshift and polariton trapping

##### 2.5.3.1 Potential landscape

##### 2.5.3.2 Trapped polariton condensates

#### 2.5.4 Spin of polaritons

## 3 Experimental procedures

### 3.1 Introduction

### 3.2 Trapped polariton spin: state of the art

### 3.3 Experimental setup

#### 3.3.1 Photoluminescence

#### 3.3.2 Real space spectroscopy

3.3.3 K-space spectroscopy

3.3.4 Microcavity sample

3.3.5 Arbitrary pattern generator

3.3.5.1 Error diffusion dither

3.3.6 Trapped polariton condensates

3.3.7 Polarization resolved spectroscopy

3.3.7.1 Excitation

3.3.7.2 Collection

3.3.7.3 Fast response setup

3.3.7.4 PMT photosensors

## 4 Results

4.1 Temperature dependance on degree of polarization

4.1.1 Spin resolved energy-real space imaging

4.2 Time and spin resolved measurements

4.2.1 Spin flips

## 5 Conclusions and perspectives

## 6 References

# 1 Introduction

The need to simulate and understand strongly correlated states of matter has given rise to the desire to model and study condensed matter phenomena. Engineering Hamiltonians in controlled systems is a useful tool for this kind of study. Controlled systems such as ultracold atoms[1], array of photonic waveguides[2] and polaritons[3] allow the manipulation of density, temperature and band structure in the case of lattice systems[4]. In all of the mentioned systems (and more), the thermal de Broglie length is comparable or even larger than the average distance between particles resulting to wavefunction overlap. In this environment, Bose statistics play a significant role in describing the fluid systems while fermi distributions diminish in importance. The majority of experiments and theoretical simulations in the field of many-body physics use material particles such as atoms and electrons. In recent years, there is a trend in considering photons as the particles suitable for studying condensed matter phenomena, provided that strong non-linearities and condensations emerge. Photon-photon interactions give rise to a fluid-like behavior in a many-photon system. Systems in the strong coupling regime are particularly promising for obtaining the non-linear interaction required for collective behaviour.

Exciton-polaritons (polaritons) are quasiparticles that emerge from strong light-matter interaction. A GaAs microcavity featuring a wide range of negative detunings is used to achieve strong light-matter coupling. Polaritons, being light-matter hybrids have strong bosonic characteristics while exhibiting strong non-linearities. Owing to their small effective mass, they are an excellent candidate for studying condensed matter phenomena, as they form condensate similar to Bose-Einstein condensates at particularly low temperature-to-density ratio. They decay by emitting light containing all information about the polaritonic state such as energy, momentum and spin, making them easily accessible. Polariton condensates emit coherent light when the excitation power is above a certain threshold. A Ti:Sapphire continuous wave laser tuned to 760nm acts as the pump beam. When excited, the quantum wells placed into the cavity produce a high density of excitons that spatially coincide with the projected pump beam. By taking advantage of the potential landscape generated by the exciton-exciton interactions, we create optical traps through the manipulation of the pump beam geometry. Trapped polariton condensates are delocalized from the excitonic pumps thus showing greater stability and lower blueshift. Moreover, they are less affected by the decoherence and spin noise of the excitonic pumps. By controlling the ellipticity of the elliptically polarized excitation beam, we tune the spin polarization of trapped polariton condensates.



In this thesis, two experimental setups were developed in order to explore the temperature dependence of the degree of polarization in optically trapped polariton condensates in pursuit of real world applications that require room temperature. The first experiment uses a single high dynamic range CCD sensor coupled with a spectrometer. Light emitted by trapped polariton condensates is analyzed to its right and left handed circularly polarized components. The components are then independently projected to the CCD sensor for determining the degree of polarization. The second experiment uses two separate photomultiplier tubes as sensors (one for each component) while utilizing the same polarization resolved setup design. With the second setup, we are able to determine the momentary degree of polarization and thus study the spin flips of polariton condensates. At low temperatures, we detect spin polarization  $P = (I_{\sigma+} - I_{\sigma-}) / (I_{\sigma+} + I_{\sigma-})$  of more than 85% while at 90K it does not drop below 75%. Finally, we study stochastic spin flips of polariton condensates when excited by linearly polarized light and the effect of temperature on the spin flip rate. We are able to measure spin flip at the record temperature of 90K.

## 2 Basic theory

### 2.1 Introduction

This chapter is a basic overview of the theoretical background required for understanding matter and light confinement as well as light-matter coupling in semiconductor microcavities. In the first section, there is an introduction about matter confinement and excitons while the second section describes photon confinement and light-matter coupling. Finally, the third section describes some of the properties of emerging polaritons and polariton condensates as well as the effect of various pumping procedures.

### 2.2 Matter

#### 2.2.1 Excitons

In semiconductors, the electrons in the conduction band and the holes in the valence band have opposite charges and they interact with each other by coulomb interactions. This interaction is reminiscent of the interaction between a proton and an electron forming a hydrogen atom. Due to this interaction, the electron-hole pair form a new quasiparticle: the exciton. The strength of the interaction is called the *binding energy* of the exciton. The wavefunction of the exciton satisfies the hydrogen-like Schrödinger equation. Solving this Schrödinger equation reveals that the binding energy is given by:

$$E_b^n = \frac{R^*}{n^2}$$

where  $n$  is the energy state number and  $R^*$  is the effective Rydberg energy given by:

$$R^* = \frac{\mu e^4}{2\hbar(4\pi\epsilon_0\epsilon)^2}$$

where  $\mu = [(m_e^*)^{-1} + (m_h^*)^{-1}]^{-1}$  is the reduced mass of the electron-hole pair, and  $\varepsilon$  is the relative permittivity of the material. The binding energy of the exciton determines the stability of the exciton. For thermal energy of  $K_B T > E_b$ , the probability of excitons dissociating to electrons and holes is larger than the probability of exciton staying bound. Excitons in bulk GaAs have a binding energy of about 4.2meV[5].

Electrons and holes are fermions. A good approximation for a single exciton is that it is a boson (as it has a spin number of either 0 or 1). An ideal exciton is considered to be an electrically neutral quantum of electronic excitation energy travelling through the periodic structure of a crystal. As such, excitons can be created and destroyed from the Fermi level. The reason I wrote that excitons are by a good approximation bosons is that for large enough densities, they have fermionic characteristics due to the average distance between them being smaller than their *Bohr radius*. Similarly to the hydrogen model, the Bohr radius is given by:

$$a_B^* = \frac{\hbar}{\sqrt{2\mu R^*}} = \frac{\hbar^2 4\pi \varepsilon_0 \varepsilon}{\mu e^2}$$

For average distance between excitons smaller than their Bohr radius, the fermionic characteristics start to manifest since the Coulomb interactions between electrons and holes becomes screened by the adjacent carriers. Under these conditions, the excitons behave more like an electron-hole plasma. The critical density in which excitons undergo this phase transition is called *Mott density*. The Mott density is related to Bohr radius by  $N_{Mott} \propto 1/a_B^{*3}$ . In bulk GaAs, the Bohr radius is about 11.6nm.

#### 2.2.1.1 Exciton energy

The energy of excitons differs from that of the hydrogen atom since excitons are realized inside a crystal whose effect must be taken into account in order to define the total exciton energy. The components that make the exciton energy is the energy dispersion of electrons and holes inside the crystal, and the kinetic energy of the center of mass. The Hamiltonian of the exciton can be written as the combination of two intertwined Hamiltonians[6]:

$$H_X = H_{mc} + H_{hl}$$

where  $H_{mc}$  is the Hamiltonian of the exciton center of mass and  $H_{hl}$  is the hydrogen like hamiltonian. The kinetic energy of the exciton center of mass is determined by the

semiconductor band structure.  $H_{mc}$  yields plane wave-like eigenstates and the eigenenergies are given by:

$$E_{mc}(k) = E_g + \frac{\hbar^2 k^2}{2M}$$

where  $M = m_e^* + m_h^*$  is the exciton center of mass,  $k$  the exciton wavevector and  $E_g$  the semiconductor bandgap at  $k = 0$ .

The eigenenergy of the hydrogen-like Hamiltonian  $H_{hl}$  is the negative of the exciton binding energy:

$$E_{hl}^n = -E_b^n = -\frac{R^*}{n^2}$$

The total energy of the exciton inside the bulk crystal is the sum of  $E_{mc}(k)$  and  $E_{hl}^n$ :

$$E_X^n(k) = E_{mc}(k) + E_{hl}^n = E_g + \frac{\hbar^2 k^2}{2M} - \frac{R^*}{n^2}$$

Excitons can be created by absorbing a photon or destroyed by emitting one. This process mainly takes place near  $k = 0$  and from  $n = 1$ . In this case the energy of the exciton is approximated with

$$E_X \approx E_g - R^*$$

The exciton energy drops with temperature. This is due to the temperature dependence of the band gap of semiconductors. The band gap energy drops as the thermal expansion changes the lattice constant of the crystal[7]. For GaAs,  $E_g \approx 1.517eV$  at 2K and  $E_g \approx 1.420eV$  at 300K.

### 2.2.1.2 Oscillator strength

The oscillator strength is an important parameter when studying light-matter coupling. It is a magnitude that is characteristic of the strength of an optical transition. A semiclassical model of light-matter interaction will be now introduced in order to study the oscillator strength. The model is called the *charged oscillators model*. Suppose a charged oscillator

with a charge of  $e$ , a mass of  $m$ , a resonance frequency of  $\omega_0$  and a damping factor of  $\gamma$ . This oscillator is driven by a force exerted by an external polarized electrical field  $\vec{E}_0 e^{-i\omega t}$ . The movement of the charged oscillator is given by:

$$m\ddot{\vec{x}} + m\gamma\dot{\vec{x}} + m\omega_0^2\vec{x} = e\vec{E}_0 e^{-i\omega t}$$

The Fourier transformation of this relation describes the response of the oscillator to the frequency of the external field:

$$\vec{x}(\omega) = \frac{e/m}{\omega_0^2 - \omega^2 + i\gamma\omega} \vec{E}_0$$

while the dipole moment of the oscillator is

$$\vec{p} = e\vec{x} = \vec{x}(\omega) = \frac{e^2/m}{\omega_0^2 - \omega^2 + i\gamma\omega} \vec{E}_0$$

Now assuming there are  $N$  oscillators per unit volume under the presence of the same electric field. The total polarization will read  $\vec{P} = N\vec{p}$ . The electric displacement  $\vec{D}$  of the system is by definition:

$$\vec{D} = \varepsilon_0 \vec{E} + \vec{P} = \varepsilon_0 \left( 1 + \frac{Ne^2}{\varepsilon_0 m} \frac{1}{\omega_0^2 - \omega^2 + i\gamma\omega} \right) \vec{E}_0$$

And by using  $\vec{D} = \varepsilon_0 \varepsilon \vec{E}$  we get

$$\varepsilon = 1 + \frac{f}{\omega_0^2 - \omega^2 + i\gamma\omega}$$

where  $f = \frac{Ne^2}{\varepsilon_0 m}$  is the oscillator strength of the system. It determines how strong the oscillators respond to the external field.

To transition from this classical model to describing exciton interaction with the electromagnetic field, we introduce the transition dipole matrix element [6] using the electric dipole approximation for the dielectric function.

$$H_X^D = \langle X | H_X^D | 0 \rangle$$

with  $|X\rangle$  and  $|0\rangle$  corresponding to the exciton state and the recombined state respectively. The oscillator strength of the transition now reads:

$$f = \frac{2N\omega_X}{\varepsilon_0\hbar} |H_X^D|^2$$

where  $\omega_X$  is the exciton resonance frequency, analogous to  $\omega_0$  of the classical model. The oscillator strength has dimensions of energy squared. The transition dipole matrix element is used to describe long-range interactions and it is applied between Wannier functions.. Experimentally, the oscillator strength is determined by the longitudinal-transverse [8](optical phonon)splitting  $\omega_{LT}$  due to the long range coulomb interactions and is connected to the dipole matrix element. The oscillator strength is in terms of  $\omega_{LT}$  reads:  $f = 2\hbar\omega_{LT}\hbar\omega_0$ .

### 2.2.1.3 Quantum wells

One of the most significant nanostructures required to design nanoelectronic and nano photonic devices are quantum wells (QWs), quantum wires and quantum dots . They are used to confine particles or quasi particles in space. Quantum dots confine particles in a single point (0D), quantum wire in 1D and QWs in 2D. For this thesis, only QWs are of interest. Regarding light-matter coupling, they are useful for confining matter in the same space as confined light although they have some interesting effects on excitons which I will touch on this subsection.

QWs utilize a potential well in order to confine the particles. In order to create this kind of potential, at least two materials with different band gaps are needed. The material with the lower band gap is sandwiched between the materials with higher band gap. Figure 2.1 depicts a schematic of such structure with the corresponding energy diagram for the valence and conduction band. The depth of the QW is determined by the difference between the two band gaps and the width is determined by the physical width of the sandwiched material.

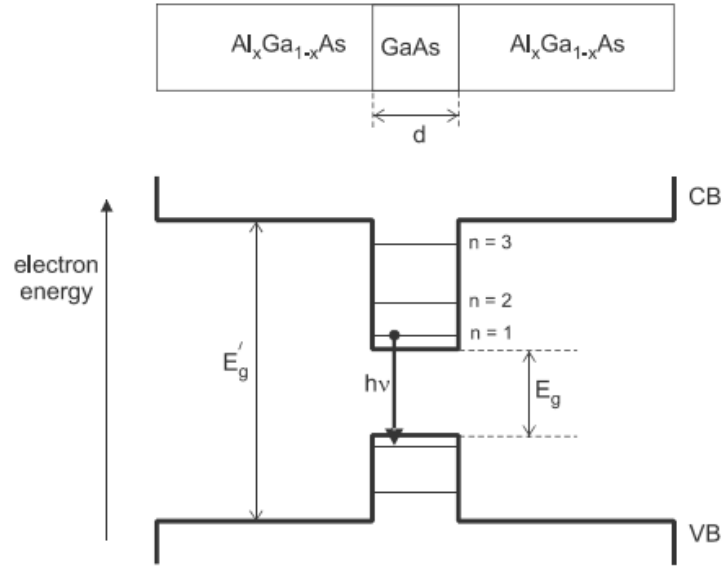


Figure 2.1.: Formation of a quantum well and the corresponding energy diagram.

In order for quantum effects to take place (for example quantized energy states), the width (sometimes referred as length) is in the order of tenths of Angstroms. Assuming the growth direction of the device is in the  $z$  axis, carriers move only along the  $x$ - $y$  plane. The average distance between electrons and holes decrease and thus the binding energy increases. Specifically, [9] calculated that the binding energy of an  $\text{GaAs-Al}_x\text{Ga}_{1-x}\text{As}$  QW (for  $k=0$ ) is given by:

$$E_b^{n^{2D}} = \frac{R_{xy}^*}{\left(n - \frac{1}{2}\right)^2}$$

while the exciton energy is:

$$E_X^{n^{2D}}(k) = E_g + \frac{\hbar^2 k_{||}^2}{2M_{||}} - \frac{R_{xy}^*}{\left(n - \frac{1}{2}\right)^2}$$

with ' $||$ ' referring to the  $x$ - $y$  plane. Compared to bulk, binding energy is four times larger in the 2D case [10]. The result is that the excitons, in the case of  $\text{GaAs-Al}_x\text{Ga}_{1-x}\text{As}$  QW, do not dissociate even at room temperature[11].

The confinement of matter in a QW is usually referred to a particle in a box. Solving the Schrödinger equations for this problem, reveals that the eigenenergies are:

$$E_n = \frac{\hbar^2 k_z^2}{2m^*} \text{ with } k_z = \frac{n\pi}{z}, n = 1, 2, 3, \dots$$

were  $m^*$  is the effective mass of the carrier. Note that holes have negative effective mass. The wavevector  $k_z$  refers to the growth direction were,  $z$  is the width of the well. The effective mass of the carrier is extracted by the curvature of the QW energy dispersion. Specifically, it is given by:

$$\frac{1}{m^*} = \frac{1}{\hbar^2} \frac{d^2 E(k)}{dk^2}$$

This relation shows that the effective mass of the carrier is inversely proportional to the curvature of the energy dispersion.

As shown in figure 2.2, the energy at  $k=0$  is split between the heavy holes and the light holes. This behaviour is called *spin orbit splitting*. In **bulk** GaAs, the conduction bands orbital is s-type (angular momentum quantum number  $l=0$ ). And the valence bands is p-type ( $l=1$ ). For electrons with spin  $s = \pm 1/2$ , the magnetic quantum number of the conduction band is from  $J_{min} = |0 \mp s|$  to  $J_{max} = |0 \pm s|$  with  $J_{total} = 0 \pm 1/2 = \pm 1/2$  with double degeneracy. For the valence band, from  $J_{min} = |-1 \mp s|$  to  $J_{max} = |1 \pm s|$ . Thus, the valence band splits into two sub-bands :  $p_{3/2}$  and  $p_{1/2}$ , with  $p_{3/2}$  being four-fold degenerate and  $p_{1/2}$  being double degenerate. In a **quantum well**, there is no inversion symmetry in the  $z$ -direction as is for bulk. Lifting the inversion symmetry, the degeneracy of the valence band is also lifted[12] with projections  $J_z = \pm 3/2$  and  $J_z = \pm 1/2$  for  $J_{total} = 3/2$  and  $J_z = \pm 1/2$  for  $J_{total} = 1/2$  with  $J_z = \pm 3/2$  representing the heavy holes and  $J_z = \pm 1/2$  representing the light holes.



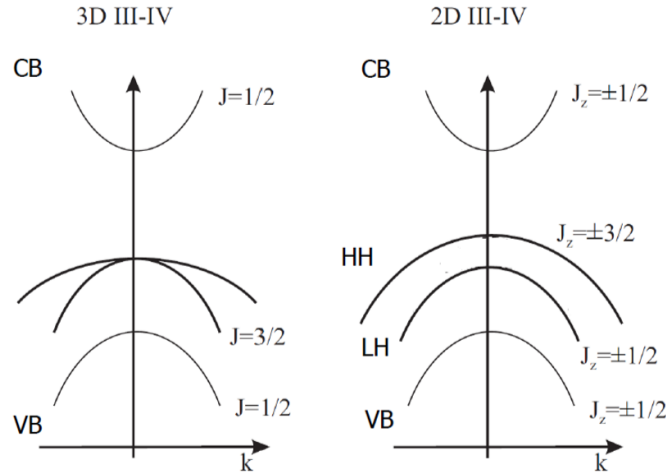


Figure 2.2. Comparison of band structure of bulk semiconductor (left) and quantum well (right). The lack of inversion symmetry in the  $z$ -direction lifts the degeneracy thus creating spin orbit splitting.

## 2.3 Light

While confinement of matter using QWs is covered in the previous section, this section covers the confinement of light. A cavity consists of two mirrors facing each other. A typical use of cavities is in laser emitters. The simplest laser cavity consists of an ideally perfect mirror facing a partially reflective mirror. The active medium is located between the two mirrors. Depending on the length of the cavity (spacing between mirrors), light field with certain wavelengths is able to have its nodes at the surface of the mirrors. Lasing amplifies these fields called surviving modes as all the other modes interfere destructively. Here, a semiconductor device called a microcavity (MC) is used. The same principle applies. The mirrors consist of alternating layers of semiconductor materials with different refractive indices to each other. This device is called distributed bragg reflector (DBR). The optical path through the layers is the same for a specific wavelength of light: the *Bragg wavelength*  $\lambda_0$ . The width of each layer is designed to provide the aforementioned optical path of  $\lambda_0/4$ . Constructive and destructive interference of the reflected light generates a spectral reflectivity behaviour called the *stopband*. Two such DBRs sandwich a cavity consisting of semiconductor material and the active medium is placed in the antinodes of the electromagnetic field. This arrangement makes a *microcavity* and it is used to confine and amplify light in the same area as the active region.

### 2.3.1 DBRs

DBRs are complex multilayered systems. It is convenient to simulate light propagation in such systems using the transfer matrix method. In order to derive the transmission and scatter matrices, let us define the electric field of a generic propagating wave. Solving the Helmholtz equation:

$$\nabla^2 \vec{E} = \mu \varepsilon \frac{\partial^2 \vec{E}}{\partial t^2}$$

where  $\varepsilon$  is the dielectric constant that includes gain and loss and  $\mu$  the magnetic permeability of the medium, the electric field can be written as:

$$\vec{E}_{(x,y,z,t)} = \hat{e} E_0 U_{(x,y)} e^{j(\omega t - \tilde{\beta} z)}$$

where  $\hat{e}$  is the unit vector indicating the polarization direction,  $E_0$  is the magnitude of the field,  $U_{(x,y)}$  is the normalized electric field profile with  $\int |U|^2 dx dy = 1$ .  $\tilde{\beta}$  is the complex propagation constant which includes the transverse modal gain  $\langle g \rangle_{xy}$  and internal modal loss  $\langle a_i \rangle_{xy}$ .  $\tilde{\beta}$  reads:

$$\tilde{\beta} = \beta + j\beta_i = \beta + \frac{j}{2}(\langle g \rangle_{xy} - \langle a_i \rangle_{xy})$$

where  $\beta = 2\pi\bar{n}/\lambda$  is the real part of  $\tilde{\beta}$  and  $\bar{n}$  is the effective refractive index.

Suppose  $a_j$  is the normalized amplitude of the field with magnitude equal to the square root of power flow and phase equal to the electric field:

$$a_j = \frac{E_0}{\sqrt{2n_j}} e^{-j\tilde{\beta}z}.$$

Incident waves are called inputs and reflected waves are called outputs. By multiplying the normalized amplitude of an input wave  $a_j$  with its conjugate, we get the power flowing in the positive direction of the z-axis:  $a_j a_j^* = P_j^+$ . The normalized amplitude of output waves is noted  $b_j$ . The total power flow at port  $j$

$$P_j = a_j a_j^* - b_j b_j^*$$

For linear optics, the outputs are linearly related to the inputs. This allows the creation of matrix formalism that expresses the outputs as weighted combination of inputs:

$$b_i = \sum_j S_{ij} a_j$$

with  $S_{ij}$  called the scattering coefficients. To determine one of the  $S_{ij}$ , all of the other inputs must be zero so that there is no reflections from other inputs to the network. An example of a two port scattering junction would be noted as:

$$\begin{bmatrix} b_1 \\ b_2 \end{bmatrix} = \begin{bmatrix} S_{11} & S_{12} \\ S_{21} & S_{22} \end{bmatrix} \begin{bmatrix} a_1 \\ a_2 \end{bmatrix}$$

$S_{11}$  and  $S_{22}$  refer simply to the normalized amplitudes of the reflected field  $r_{12}$  and  $r_{21}$  respectively, where  $r_{ij}$  refers to the reflection of the beam on an interface of two materials with refractive indices  $n_i$  and  $n_j$ . Normalized power for the reflections is  $|S_{11}|^2$  and  $|S_{22}|^2$ .  $S_{12}$  and  $S_{21}$  represent the amplitude and the phase in the form of complex numbers of the output that is created by an input. In general,  $|S_{ij}|^2$  represents the fraction of power at the port  $i$  that is generated due power at the port  $j$ .

As the scatter matrix relates normalized inputs to the outputs, the *transfer matrix* relates the inputs and outputs of a given port to those of other ports. The transmission matrix is defined as:

$$\begin{bmatrix} A_1 \\ B_1 \end{bmatrix} = \begin{bmatrix} T_{11} & T_{12} \\ T_{21} & T_{22} \end{bmatrix} \begin{bmatrix} A_2 \\ B_2 \end{bmatrix}$$

where  $A_i$  are forward propagating waves and  $B_i$  are backward propagating waves. The relation between the transfer matrix elements with the ones of the scatter matrix is:  $A_1 = a_1$ ,  $B_1 = b_1$ ,  $A_2 = b_2$ ,  $B_2 = a_2$ . Transfer matrices are convenient for describing layered and periodic optical systems like DBRs as they can be cascaded by simple matrix multiplication. For calculating the reflectivity spectra of a DBR, it is enough to find the transfer matrix of one period of alternating semiconductor layers. Specifically, one period consists of the transfer matrix of a dielectric interface, free propagation in the first

semiconductor with length  $L_1$ , another dielectric interface and another free propagation with length  $L_2$ . The scatter matrix of a dielectric interface with a material of  $n_1$  to the left and  $n_2$  to the right is:

$$S_{11} = \left. \frac{b_1}{a_1} \right|_{a_2=0} = -r_1 \quad \text{with} \quad -r_1 = \frac{n_1 - n_2}{n_1 + n_2}$$

$$S_{22} = \left. \frac{b_2}{a_2} \right|_{a_2=0} = r_2 \quad \text{with} \quad r_2 = -(-r_1)$$

$S_{12} = S_{21} = t$  with  $t = \sqrt{1 - r_1^2}$  the transmittance assuming no scattering loss. For normal incidence plane wave,  $t = 2(n_1 n_2)^{1/2} / (n_1 + n_2)$ . The scatter and transfer matrices now read:

$$S_{d1} = \begin{bmatrix} -r_1 & t \\ t & r_1 \end{bmatrix} \quad \text{and} \quad T_{d1} = \begin{bmatrix} 1 & -r_1 \\ -r_1 & 1 \end{bmatrix}.$$

To transform from the  $S$  matrix to the  $T$  matrix we use:

$$T = \frac{1}{S_{21}} \begin{bmatrix} 1 & -S_{22} \\ S_{11} & -\det S \end{bmatrix}$$

For free propagation in a medium with width  $L_1$ , the scatter matrix is:

$$S_{pr1} = \begin{bmatrix} 0 & e^{-j\widetilde{\beta}_1 L_1} \\ e^{-j\widetilde{\beta}_1 L_1} & 0 \end{bmatrix} \quad \text{and the transfer matrix is:} \quad T_{pr1} = \begin{bmatrix} e^{j\widetilde{\beta}_1 L_1} & 0 \\ 0 & e^{-j\widetilde{\beta}_1 L_1} \end{bmatrix}.$$

The combined system with the of the dielectric interface and the propagation in the material can now be extracted with a simple matrix multiplication on  $T_{d1} * T_{pr1}$  :

$$T_{12} = \frac{1}{t_{12}} \begin{bmatrix} e^{j\widetilde{\beta}_2 L_2} & r_{12} e^{-j\widetilde{\beta}_2 L_2} \\ r_{12} e^{j\widetilde{\beta}_2 L_2} & e^{-j\widetilde{\beta}_2 L_2} \end{bmatrix}$$

with  $t_{12} = \sqrt{1 - r_{12}^2}$ . The transfer matrix  $T_{12}$  represents the dielectric interface of from material 1 to material 2 and the propagation in the material 2.  $T_{21}$  is produced using the same reasoning:

$$T_{21} = \frac{1}{t_{21}} \begin{bmatrix} e^{j\tilde{\beta}_1 L_1} & r_{21} e^{-j\tilde{\beta}_1 L_1} \\ r_{21} e^{j\tilde{\beta}_1 L_1} & e^{-j\tilde{\beta}_1 L_1} \end{bmatrix}.$$

The transfer matrix of one period is:

$$T_{per} = \frac{1}{t^2} \begin{bmatrix} e^{j\phi^+} - r^2 e^{-j\phi^-} & r e^{-j\phi^+} - e^{j\phi^-} \\ r e^{j\phi^+} - e^{-j\phi^-} & e^{-j\phi^+} - r^2 e^{j\phi^-} \end{bmatrix}$$

Where  $\phi_{\pm} = \tilde{\beta}_1 L_1 \pm \tilde{\beta}_2 L_2$ . The total matrix of the DBR is  $T_{DBR} = T_{per}^m$  where  $m$  is the number of periods. To get the reflectivity of a certain wavelength, it is convenient to convert the total transfer matrix back to its respective scatter matrix. The reflected power  $|r|^2 = S_{11}^2$ . Performing this calculation in a range of wavelength, yields the reflectivity spectrum of the DBR.

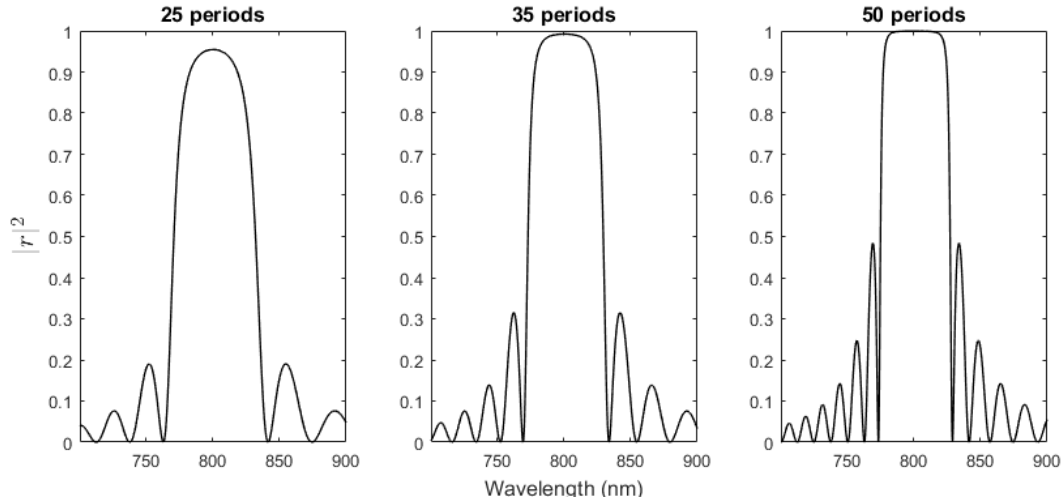


Figure 2.3. DBR reflectivity spectra for three different number of periods: 25 periods (left), 35 periods (middle) and 50 periods (right). The materials used for this simulation GaAs with  $n_{\text{GaAs}}=3.95$  and  $\text{Al}_{0.15}\text{Ga}_{0.85}\text{As}$  with  $n_{\text{AlGaAs}}=3.61$ . The Bragg wavelength is set to 800nm. One period consist of one pair of alternating GaAs and  $\text{Al}_{0.15}\text{Ga}_{0.85}\text{As}$ .

Figure 2.3 compares the calculated reflectivity spectrum of three DBRs with different number of periods. They consist of the same two alternating materials. The effect of period number at the Bragg wavelength is depicted in figure 2.4. The magnitude of reflection coefficient, provided that the number of periods is sufficient, can reach values larger than 0.9999. This makes the DBS the perfect mirror for fabricating microcavities.

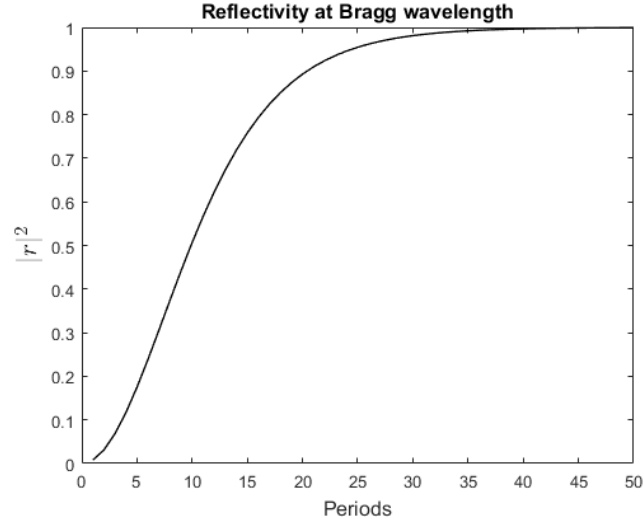


Figure 2.4. Relation between magnitude of reflectivity at the Bragg wavelength and number of alternating pairs (periods). Reflectivity reaches magnitude of larger than 0.9999 at fifty periods.

### 2.3.2 Planar microcavities with DBRs

When an optical cavity with length comparable to the wavelength of incident light is sandwiched between two mirrors, the entire structure makes a *microcavity*. The purpose of the cavity is to confine and enhance the electric field inside the medium, where the quantum wells are placed. For exceptional quality microcavities, we use DBRs instead of metallic mirrors. The advantage of using DBRs instead of traditional metallic mirrors is large reflectivity values they offer compared to their metallic counterparts. High reflectivity values yield large 'Q-factors'. Since even with DBRs, the reflectivity is not exactly 1, the intensity of the cavity mode decays with time as photons escape from the DBRs. A dimensionless parameter called the *Q-factor* describes the ratio between energy stored in the cavity and the energy dissipated for every optical cycle multiplied by  $2\pi$ :

$$Q = \left| \omega_C \frac{U}{dU/dt} \right|$$

where  $\omega_C$  is the frequency of the cavity mode,  $U$  is the electromagnetic energy stored inside the cavity and  $dU/dt$  is the loss rate. Solving for  $U$  yields:

$$U(t) = U_0 e^{-\omega_C/Q} = U_0 e^{-t/\tau}$$

with  $U_0$  the injected energy and  $\tau = Q/\omega_C$  the lifetime of the cavity mode. Cavity lifetime is the time that a photon spends in the cavity before it escapes. The electromagnetic energy  $U(t)$  and the amplitude of the electric field  $|E(t)|^2$  are linearly related so the electric field can be written as

$$U(\omega) \propto |E(\omega)|^2 \propto \frac{1}{(\omega - \omega_C)^2 + (\omega_C/2Q)^2}$$

This distribution has full-width-half-maximum (FWHM)  $\Delta\omega = \omega_C/Q$ . Solving for Q yields:

$$Q = \frac{\omega_C}{\Delta\omega} = \frac{E_C}{\Delta E} \approx \frac{\lambda_C}{\Delta\lambda}.$$

The approximation is valid for  $\lambda_C \gg \Delta\lambda$ . In the case of microcavities,  $\lambda_C$  is the Bragg wavelength and the condition holds true.

As the electromagnetic field is confined inside the cavity, it is many times more intense than the incident light (figure 2.5). Both of these cavity effects (confinement and amplification) are crucial for achieving strong coupling between photons and excitons as we will see in the next section.

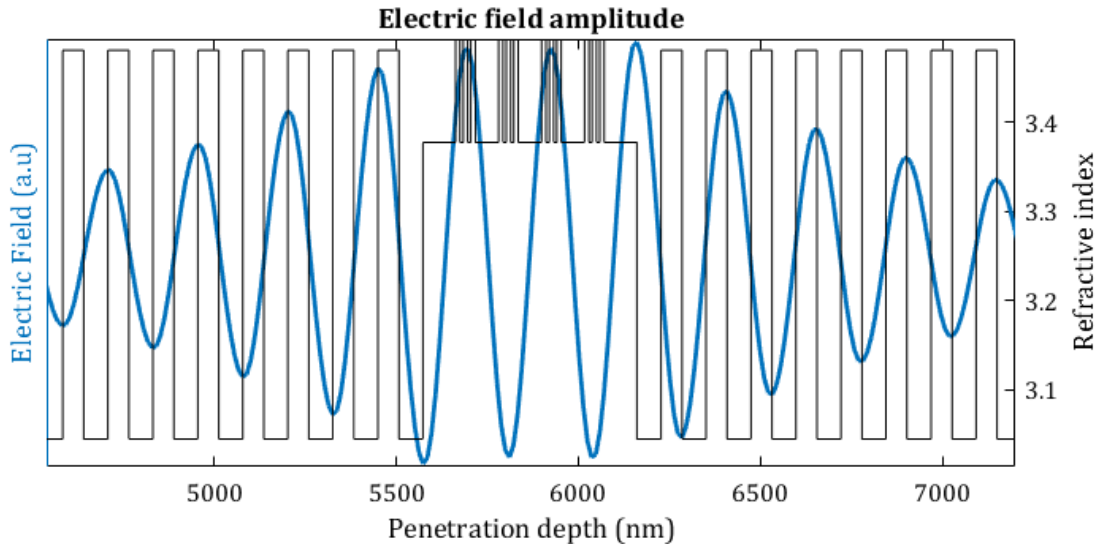


Figure 2.5: Electric field magnitude (blue) versus penetration depth in a microcavity (black)

Applying the transfer matrix method to a cavity with two DBRs on either side, revivals a reflectivity dip at the Bragg wavelength as seen in figure 2.6. Note that the cavity length is tuned to the same wavelength  $\lambda_0$  as the DBRs; the Bragg wavelength:

$$L_C = m \frac{\lambda_0}{2n_C}$$

where  $n_C$  is the refractive index of the cavity and  $m$  an integer. The reflectivity dip is called the *cavity mode*. As we have already discussed, the cavity Q-factor depends on the reflectivity of the mirrors (in this case the DBRs). Figure 2.7 compares the period number of the DBRs (and thus the reflectivity) with the FWHM of the dip on the reflectivity at the Bragg wavelength (and thus the Q-factor). The reflectivity of DBRs is exponentially dependent on the number of pairs and by induction the Q-factor. Using the same materials, the Q-factor of the MC with 15 pairs is 445 while for 50 pairs it is 5,839,416. This tremendously affects the samples ability for strong coupling. The downside is that, experimentally, the emitted light is significantly reduced and hence it is more difficult to detect and analyze it.

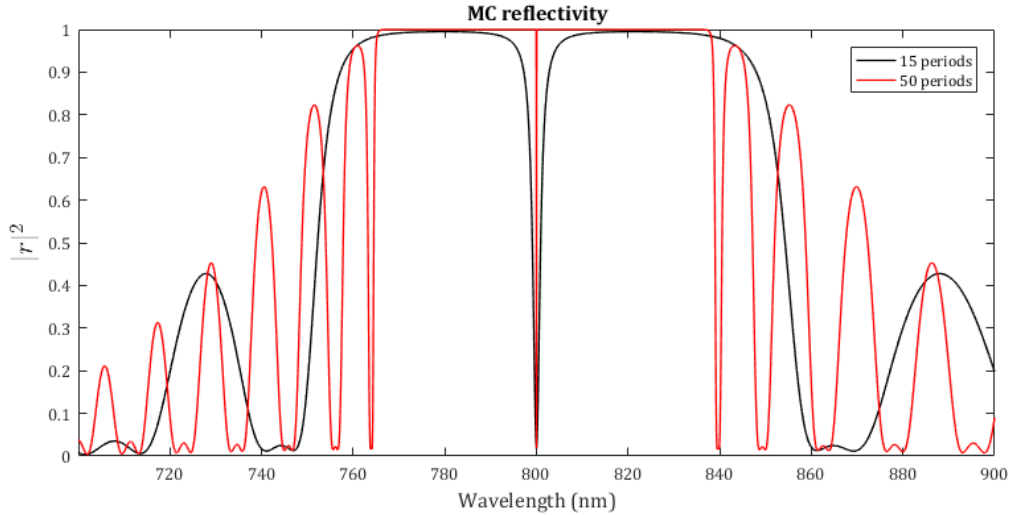


Figure 2.6. Reflectivity spectrum for two microcavities, each consisting of two identical DBRs with 15 periods and 50 periods respectively. On both, the cavity length is  $L_c = 5\lambda_0/2n_c$ . The device consists of alternating layers of GaAs with  $n_{\text{GaAs}}=3.48$  and  $\text{Al}_{0.15}\text{Ga}_{0.85}\text{As}$  with  $n_{\text{AlGaAs}}=3.04$ . The Bragg wavelength is 800nm



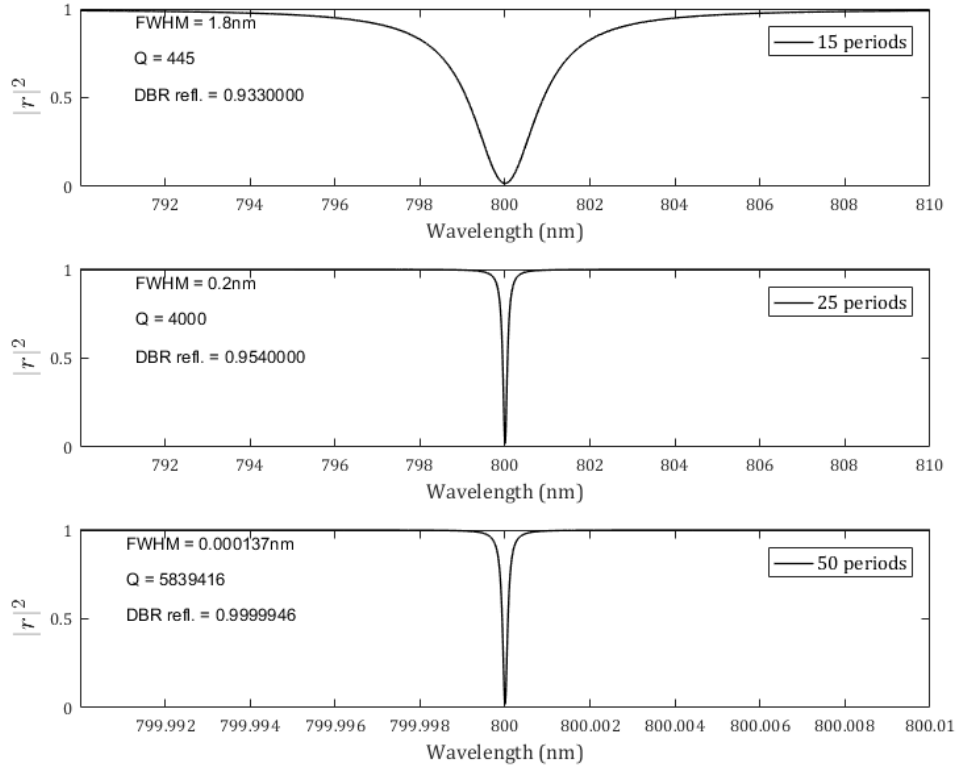


Figure 2.7. Reflectivity spectrum near the Bragg wavelength of three MCs with different number of pairs. 15 pairs (top), 25 pairs (middle), 50 pairs (bottom). This simulation is performed using the transfer matrix method. All MCs consist of alternating layers of GaAs with  $n_{\text{GaAs}}=3.48$  and  $\text{Al}_{0.15}\text{Ga}_{0.85}\text{As}$  with  $n_{\text{AlGaAs}}=3.04$ . The Bragg wavelength is 800nm.

As the electromagnetic wave is confined inside the cavity, its energy dispersion differs from that of the free propagating photons. This is due to the quantization of the  $k_z$  wavevector (the microcavity is grown along the  $z$ -axis and light propagates parallel to the growth axis). The components of the  $k$  vector along the  $xy$  plane are the same as the ones of the free propagating wave. The quantization of the  $k_z$  wavevector reads as:

$$k_z = \frac{2\pi}{L_C}$$

And the energy dispersion of the electromagnetic field is given by:

$$E_{Ph} = \frac{c\hbar}{n_C} 1 + \sqrt{\frac{k_{\parallel}^2}{k_z^2}} = \frac{c\hbar}{n_C} \frac{2\pi}{L_C} + \frac{c\hbar}{2n_C} \frac{L_C k_{\parallel}^2}{2\pi} = E_0 + \frac{\hbar^2 k_{\parallel}^2}{2m_{Ph}^*}$$

where  $m_{Ph}^* = \hbar n_C / c L_C$ , is the effective mass of the photon. Figure 2.8 shows the parabolic relation between energy and  $k_{||}$ . The effective mass is related to the curvature (the second derivative) of this parabola-like curve: Higher curvature means smaller effective mass. As we will see in the next section, the  $k_{||}$  wavevector does not affect the energy of excitons in the same range. This means that the effective mass of excitons is much larger than that of the cavity photons. In fact, the effective mass of excitons is four orders of magnitude larger while electrons have effective mass five orders of magnitude larger. The wavevector  $k_{||}$  is

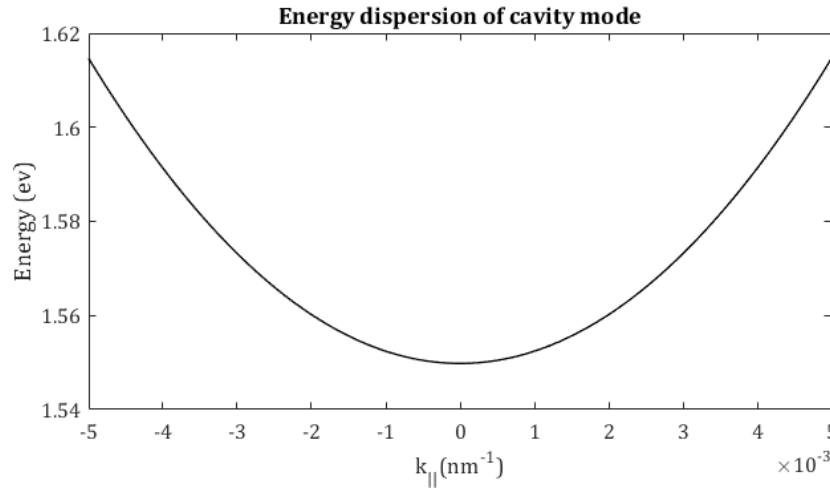


Figure 2.8. Energy dispersion of cavity photons.

directly related to the incidence angle (or the emission angle) through:

$$k_{||} = \frac{E_{Ph}(k)}{c\hbar} \sin(\theta)$$

where  $\theta$  is the incidence or the emission angle. This renders the access of the microcavity system ideal for experimental study since angle resolved spectroscopy (an easy to access experimental setup) yields direct information about the energy dispersion on the cavity mode (and the polariton branches as is analyzed in the next section) .

## 2.4 Light matter coupling

In bulk semiconductor materials, exciton-polaritons (polaritons) are quasiparticles that emerge from the coupling of semiconductor excitons with photons, therefore becoming eigenstate of the system. These bulk polaritons are annihilated at the surface of the semiconductor material, transforming into photons that carry all information of their previous state. In semiconductor microcavities, polaritons are formed by coupling excitons from the active material (quantum wells) with cavity photons. This thesis studies exciton polaritons in microcavities and from now on they will be referred as polaritons. Polaritons inherit characteristics from both excitons and photons. They are bosons so, given the right conditions, they form macroscopical polariton condensations. Polariton condensates emit coherent light (polariton lasing).

The next sections will provide a more in-depth description of polaritons and polariton condensates.

### 2.4.1 Quantum description of light

Light can be described as a classical optical field. In order to describe it as a quantum object, we reformulate it as a particle that corresponds to an excitation of the field. This is called *second quantization*. Treating photons and excitons as quantized fields, the coupled-quantum oscillator model is fit for the description of the strong coupling regime.

Firstly, we choose a set of orthogonal states  $\{|\phi_i\rangle\}$  as the basis. These states represent the eigenmodes of the field excitation. For  $n_i$  excitations in the  $i$ th mode  $|\phi_i\rangle$ , the state of the entire system is given by:

$$|\Psi\rangle = |n_1, n_2, \dots, n_i, \dots\rangle$$

The  $n_i$ th particle has energy equal to  $(n_i + 1/2)\hbar\omega_i$  as for the quantum oscillator. It consists of  $n_i$  excitations with energy  $\hbar\omega_i$  each (where  $\omega_i$  is the oscillator frequency at the  $i$ th state). The remainder  $(1/2)\hbar\omega_i$  is the energy of the vacuum. Creating a new excitation in the  $i$ th mode is achieved by the creation operator ( $a_i^\dagger$ ) while removing one excitation is achieved by the annihilation operator ( $a_i$ ). This means:

$$a_i^\dagger |n_1, n_2, \dots, n_i, \dots\rangle = \sqrt{n_i + 1} |n_1, n_2, \dots, n_i + 1, \dots\rangle \text{ and} \\ a_i |n_1, n_2, \dots, n_i, \dots\rangle = \sqrt{n_i} |n_1, n_2, \dots, n_i - 1, \dots\rangle$$

The number operator  $a_i^\dagger a_i$  yields the number of particles in the  $i$ th mode while it leaves the system unchanged:

$$a_i^\dagger a_i |n_1, n_2, \dots, n_i, \dots\rangle = n_i |n_1, n_2, \dots, n_i, \dots\rangle$$

Note that  $|n_1, n_2, \dots, n_i, \dots\rangle$  is an eigenstate of  $a_i^\dagger a_i$  with  $n_i$  as its eigenvalue. Finally, the physical process in which a particle in the  $i$ th state is annihilated to create another particle in the  $j$ th state is expressed by the operator  $a_j^\dagger a_i$ .

## 2.4.2 Exciton -photon coupling

For the description of coupling between excitons and photons, we will use the *coupled oscillators* model. We begin by assuming  $|X_k\rangle$  the state of an exciton with wavevector  $k$  and  $|Ph_k\rangle$  the state of a photon with wavevector  $k$ . We assume (for now, see chapter 2.5.3) low density of excitons and thus no exciton-exciton interaction. The creation operator for excitons is  $b_k^\dagger$  and the annihilation operator is  $b_k$ . Respectively the creation and annihilation operators for photons are  $a_k^\dagger$  and  $a_k$ . We set the base of the system to be  $|X_k\rangle$  and  $|Ph_k\rangle$ . The Hamiltonian that describes a non coupling system is written as:

$$H_k^0 = E_X(k)b_k^\dagger b_k + E_{Ph}(k)a_k^\dagger a_k$$

Where  $E_X(k)$  and  $E_{Ph}(k)$  is the energy of the excitons and photons respectively at the wavevector  $k$ . The states that describe the uncoupled particles are called *bare states*. They are the eigenstates of the  $H_k^0$  Hamiltonian and are written as  $|n_k^X, n_k^{Ph}\rangle$  with  $n_k^X$  and  $n_k^{Ph}$  the number of excitons and photons at with wavevector  $k$ .

For describing interaction photons and excitons that involve optical transitions, we use the interaction Hamiltonian written as:

$$H_k^{int} = g(b_k^\dagger a_k + a_k^\dagger b_k)$$

The operators  $b_k^\dagger a_k$  and  $a_k^\dagger b_k$  correspond to the creation of an exciton by absorption of a photon and the creation of a photon by the relaxation of an exciton respectively. Here,  $g$  is the coupling coefficient and is given by

$$g = \frac{1}{2} \sqrt{f} \int d\vec{r} u_{ph}(\vec{r}) u_X(\vec{r})$$

Where  $f$  is the exciton oscillator strength and the integral  $\int d\vec{r} u_{ph}(\vec{r}) u_X(\vec{r})$  is the overlap of the electromagnetic field with the wavefunction of the exciton ( $u_{ph}(\vec{r})$  and  $u_X(\vec{r})$  resp.). For this case (using a microcavity sample) the excitons are assumed to exist only in the active region so the overlap integral is determined by the penetration depth of the electromagnetic field into the DBRs and the cavity. The penetration depth is close to  $L_{eff} = L_{DBR_1} + L_{DBR_2} + L_C$ .  $L_{eff}$  represents the spreading of the electric field out of the dielectric medium. Then,  $g$  takes the form:

$$g = \frac{1}{2} \sqrt{\frac{f L_c}{L_{eff}}}$$

Now that the Hamiltonians for non interacting particles  $H_k^0$  and coupled particles  $H_k^{int}$  are defined, we can present the total Hamiltonian of the system simply as:

$$H_k = H_k^0 + H_k^{int} = E_X(k) b_k^\dagger b_k + E_{Ph}(k) a_k^\dagger a_k + g b_k^\dagger a_k + g a_k^\dagger b_k$$

With  $|n_k^X, n_k^{Ph}\rangle$  as the basis of the system, the total Hamiltonian  $H_k$  has the matrix form:

$$\begin{bmatrix} E_X(k) & g \\ g & E_{Ph}(k) \end{bmatrix}$$

By calculation the eigenvalues of the matrix, we get two eigenenergies of the system:

$$E_{LP}(k) = \frac{E_X(k) + E_{Ph}(k)}{2} - \frac{\sqrt{(E_X(k) - E_{Ph}(k))^2 + 4g^2}}{2} \text{ and}$$

$$E_{UP}(k) = \frac{E_X(k) + E_{Ph}(k)}{2} + \frac{\sqrt{(E_X(k) - E_{Ph}(k))^2 + 4g^2}}{2}$$

Which correspond to the energy dispersions on the lower and upper polariton branches of the new coupled system.

The corresponding normalized eigenvectors are:

$$\begin{bmatrix} C_X(k) \\ C_{Ph}(k) \end{bmatrix} \text{ and } \begin{bmatrix} C_{Ph}(k) \\ -C_X(k) \end{bmatrix}$$

Where

$$C_X(k) = \frac{1}{\sqrt{1 + \left( \frac{E_{LP}(k) - E_x(k)}{g} \right)^2}} \text{ and}$$

$$C_{Ph}(k) = \frac{1}{\sqrt{1 + \left( \frac{g}{E_{LP}(k) - E_x(k)} \right)^2}}.$$

$C_X(k)$  and  $C_{Ph}(k)$  are called the Hopfield coefficients and they satisfy the relation  $|C_X(k)|^2 + |C_{Ph}(k)|^2 = 1$ . Using the Hopfield coefficients, we can define the creation and annihilation operators for lower and upper polariton in terms of the bare exciton and photon operators.

$$p_k^\dagger = C_X(k)b_k^\dagger + C_{Ph}(k)a_k^\dagger \text{ and}$$

$$q_k^\dagger = C_{Ph}(k)b_k^\dagger - C_X(k)a_k^\dagger$$

The Hamiltonian of the system can now be re-expressed in the diagonalized form as:

$$H_k = E_{LP}(k)p_k^\dagger p_k + E_{UP}(k)q_k^\dagger q_k$$

The eigenstates of  $H_k$  can be expressed as  $|n_k^{LP}, n_k^{UP}\rangle$  where  $n_k^{LP}$  and  $n_k^{UP}$  are the number operators of the lower and upper polariton with wavevector  $k$  and are called *dressed states*. They are a result of exciton-photon coupling. As we have seen, the optical transitions directly involve involve the operators  $a_k$  and  $b_k$  (and their conjugates) and not  $p_k$  and  $q_k$ . However, the latter can still represent photon emission as only transitions from the states  $|n_k^{LP}, n_k^{UP}\rangle$  to  $|n_k^{LP} - 1, n_k^{UP}\rangle$  or  $|n_k^{LP}, n_k^{UP} - 1\rangle$  are allowed in the dressed-state picture. These transitions give rise to emission energies  $E_{LP}(k)$  or  $E_{UP}(k)$  to the radiation spectra[13]. The upper polariton branch and the lower polariton branch can be expressed using the Hopfield coefficients in respect to photon and exciton states as:

$$|LP_k\rangle = C_X(k)|X_k\rangle + C_{Ph}(k)|Ph_k\rangle \text{ and}$$

$$|UP_k\rangle = C_{Ph}(k)|X_k\rangle + C_X(k)|Ph_k\rangle$$

With

$|LP_k\rangle = |0, 1\rangle$  and  $|UP_k\rangle = |1, 0\rangle$  as the base of the system.

In this case, the physical meaning of  $|C_X|^2$  and  $|C_{Ph}|^2$  is the fraction of the excitons and photons of the polariton lower polariton branch LPB and inversely at the upper polariton branch UPB. We denote the detuning  $\Delta$  of the eigenenergies  $\Delta = E_{Ph} - E_X$ . Figure 2.9 shows the relation between the detuning  $\Delta$  and the eigenenergies of the LPB and UPB compared to the bare states of the exciton and the photon.

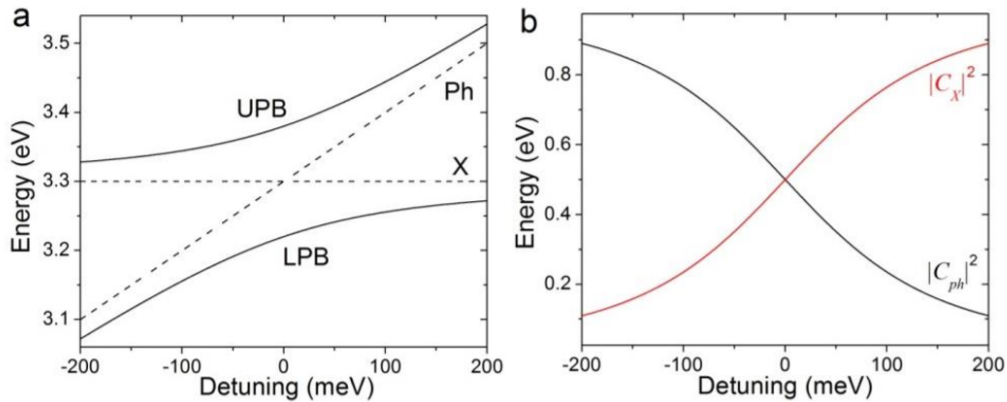


Figure 2.9: **a.** Polariton branches (solid lines) as a function of detuning, at  $k_{||}=0$  compared to exciton and photon modes (dashed lines). **b.** Fractions of excitons (red) and photons (black) of the lower polariton branch as a function of detuning at  $k_{||}=0$ . Here,  $E_x=3.3\text{eV}$  and  $g=80\text{meV}$ .

Cavity photons have quite small effective mass compared to excitons in the active media. The energy dispersion reflects that, showing that the energy of photon mode varies significantly more for a certain range of wavevectors while the energy of the exciton mode varies insignificantly for the same range of wavevectors, looking to be flat. This is true for wavevectors close to  $k_{||} = 0$  which is usual for studying polariton condensates. This means that the detuning  $\Delta$  changes with  $k_{||}$  for a given cavity. From now on, detuning refers to  $k_{||}=0$ . Figure 2.10 shows the dispersion curves of the bare and the polariton modes with for  $\Delta = -200\text{meV}$ ,  $0\text{meV}$  and  $200\text{meV}$  with Rabi splitting of  $160\text{meV}$ . With negative detuning, the UPB exhibits more exciton like behaviour compared to zero detuning while it resembles the cavity mode at positive detunings. The LPB shows opposite response. As the polariton branches approach the exciton energy their effective mass increases.

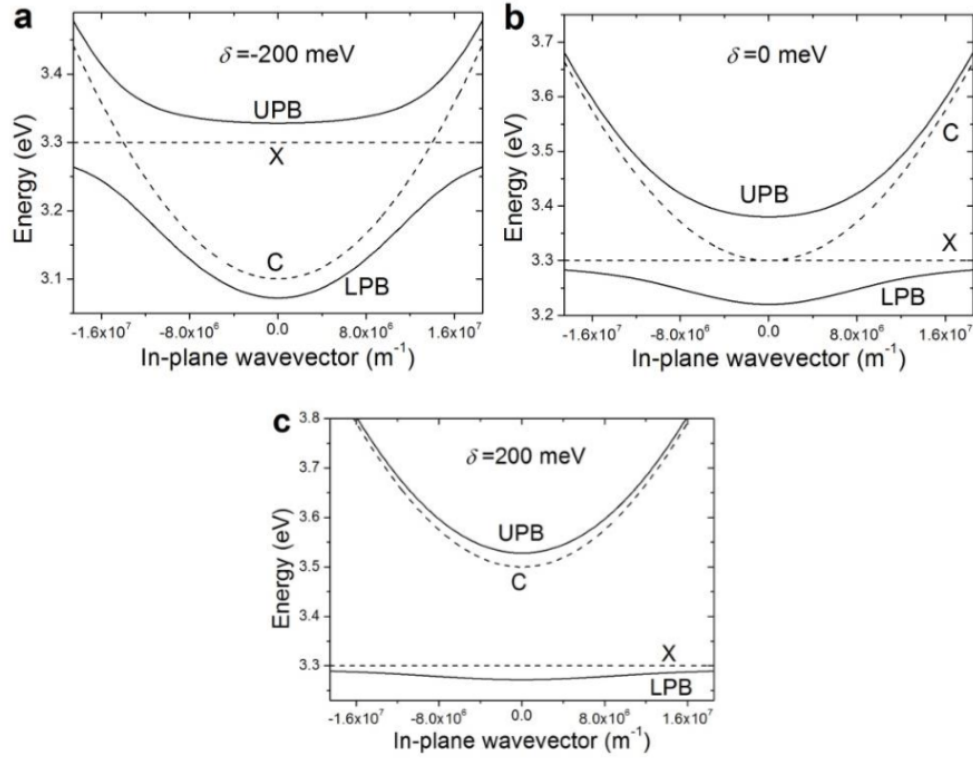


Figure 2.10. The energy dispersion the two polariton branches for **a.** negative, **b.** zero, **c.** positive detunings in a microcavity. The bare exciton and photon modes are labeled X and C (dashed lines). Parameters used:  $n_c = 2.3$ ,  $E_x = 3.3\text{eV}$ ,  $g = 80\text{meV}$ .

For more accurate description, we introduce the mode broadening of excitons and photons and study its effect on the coupling regime and Rabi splitting. An imaginary term [14] is introduced to the eigenenergies of exciton and photon  $\gamma_X$  and  $\gamma_{Ph}$  respectively. The total Hamiltonian for the coupled system now reads:

$$\begin{bmatrix} E_X(k) - \gamma_x & g \\ g & E_{Ph}(k) - \gamma_{Ph} \end{bmatrix}$$

Exciton mode broadening is due to temperature (interaction with LO phonons [15]) while photon mode broadening is the spectral linewidth of the radiation due to losses within the cavity. For photons in a microcavity  $\gamma_{Ph} = \gamma_C$  where  $\gamma_C \propto 1/Q$ . The coupling coefficient  $g$  takes into account mode broadening due to exciton-photon interactions. The new eigenenergies of the polariton branches are obtained by diagonalizing the corrected Hamiltonian:

$$E_{UP,LP}(k) = \frac{E_X(k) + E_{Ph}(k)}{2} - i\frac{\gamma_X + \gamma_{Ph}}{2} \pm \frac{\sqrt{(E_X(k) - E_{Ph}(k) - i(\gamma_X - \gamma_{Ph}))^2 + 4g^2}}{2}$$



Or

$$E_{UP,LP}(k) = E - i\frac{\gamma_X + \gamma_{Ph}}{2} \pm \frac{\sqrt{4g^2 - i(\gamma_X - \gamma_{Ph})^2}}{2}$$

With  $E = E_X = E_{Ph}$  for zero detuning. The Rabbi splitting  $\hbar\Omega_R$  in zero detuning is now corrected from  $\hbar\Omega_R = 2g$  to  $\hbar\Omega = \sqrt{4g^2 - (\gamma_X - \gamma_{Ph})^2}$ . The system is considered to be in the strong coupling regime if the Rabbi splitting formula yields a real value meaning  $4g^2 > (\gamma_X - \gamma_{Ph})^2$ . In the weak coupling regime, where  $4g^2 < (\gamma_X - \gamma_{Ph})^2$  the Rabbi splitting yields imaginary value so the energy splitting is not measurable. The coupling regime is essentially dependent on the balance between the exciton oscillator strength ( $g \propto f$ ) and the linewidths of excitons and photons. Being in the weak coupling regime does not mean that there is no polariton. In fact, the imaginary Rabbi splitting in the weak coupling regime affects the polariton linewidth.

## 2.5 Polaritons

### 2.5.1 Bose-Einstein and polariton condensation

At the microcosm, the length of the wave-function is comparable with the distance between the particles. This leads to the indistinguishability principle; particles are identical. This idea led to splitting particles into two categories: the bosons and the fermions. Bosons are described by symmetrical wave-functions and an integer number as spin. Fermions have anti-symmetrical wave-functions and semi-integer spin. The last are subject to the Pauli's principle which prohibits the coexistence at the same quantum state. In contrast, bosons can coexist at the same quantum state (constructive quantum interference), allowing the realization of Bose-Einstein condensation (BEC).

According to the BEC theory, the scattering rate in a bosonic state is increased by the existence of other bosons in this state. If  $N$  particles are in a bosonic state, the scattering rate is proportionate to  $(N+1)$ [16]. The above creates a carrier avalanche; a more populated quantum state leads to an increase in population rate at this state. This phenomenon is known as bosonic final state stimulation.

A Bose gas consists of  $N$  free non-interacting Bose particles. In thermal equilibrium, and temperature  $T$ , it is described by the Bose distribution in the momentum space as:

$$f_B(k, T, \mu) = \frac{1}{\exp\left(\frac{E_k - \mu}{k_B T}\right) - 1}$$

where  $E(k) = \frac{\hbar^2 k^2}{2m}$  is the boson dispersion function,  $k$  is the particle's wave-vector and  $\mu$  is the chemical potential, which is determined by the number of particles in the system. At the limit  $\mu \ll k_B T$  and  $e^{-k_B T} \gg 1$ , one can use the Maxwell-Boltzmann statistical approach:

$$f_{ME}(k, T, \mu) = \exp\left(-\frac{E(k) - \mu}{k_B T}\right) + 1$$

The total number of particles  $N$  is given from

$$N(T, \mu) = \sum_k f_B(k, T, \mu) = \frac{1}{\exp\left(\frac{-\mu}{k_B T}\right) - 1} + \sum_{k \neq 0} f_B(k, T, \mu) = N_{E=0}(T, \mu) + N_{E \neq 0}(T, \mu)$$

Suppose energy at the ground state  $E_0 = 0$  and  $\mu$  taking negative values increasing with density. At the limit  $\mu \rightarrow 0$ , the Bose-Einstein distribution begins to deviate, and the occupation of the fundamental state  $n_0 \approx (k_B T)/(E_0 - \mu)$  is getting very large without any limit. However, the particle number  $N_{E \neq 0}$  populating the excited states, is limited, even when  $\mu=0$  (thermodynamic limit), and is proportionate to the system's volume. For a set temperature, there are two possibilities: If the total number of particles can be distributed to the excited states, the saturation of the ground state is of the same order as the saturation of the excited states. If  $N$  is larger than the critical density:  $N_{cr} = N_{E \neq 0}(T, \mu = 0)$ , then the number of particles can populate the ground state so that the equation

$$N(T, \mu) = \sum_k f_B(k, T, \mu)$$

is met.

Einstein suggested this solution [17] taking inspiration from Bose's work [18].

Taking into account the saturation of the excited states, the extra particles start massively populating the ground state resulting in a comparable population of the latter to the

population of the whole system. The saturation of the excited states and the macroscopic saturation of the ground state is the transition called Bose-Einstein Condensation as shown in figure 2.11.

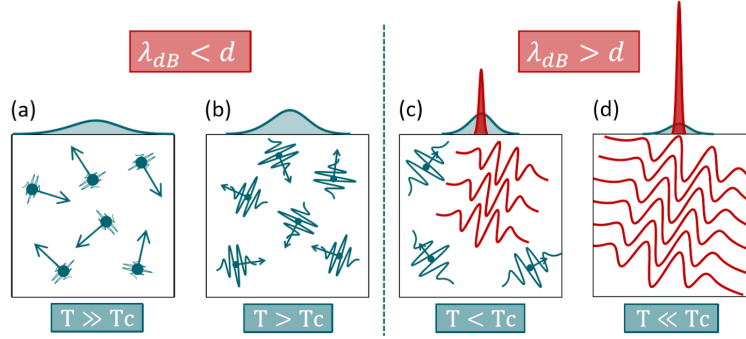


Figure 2.11: Bose-Einstein condensation: De-Broglie wavelength (wavy blue lines) grows larger relative to the average distance between particles due to temperature drop. Below  $T_c$  (vertical dashed line) the overlap of wavefunctions generates coherency and reduced linewidth.

Polaritons, being bosons, form condensates that closely resemble the Bose-Einstein condensates for exciton densities less than the Mott density. Microcavity polaritons are ideal candidates for creating condensates compared to atoms and excitons. Their effective mass is five orders of magnitude smaller than that of the electrons and they have four orders of magnitude smaller than excitons. As a result, the critical temperature for forming condensates can be in the range room temperature. Polaritons with a set wave-vector in a lattice are directly linked to the outbound photons as per the latter having the same energy and wave-vector while they propagate in an angle  $\theta$  from the growth direction. As a result, their properties can be measured with common optical experimental procedures, containing information about energy dispersion-wavevector, their population and their distribution to the energy states. Moreover, polaritons can be easily excited either by non-resonant excitation either by resonant optical excitation, changing the angle and the light beam energy. As a 2D system, there is no predicament of microcavity polaritons to present BEC transition at a finite temperature. BEC is possible in 2D systems with finite size, like in the case of this experiment. The phase diagram of polariton condensates in GaAs systems is presented in figure 2.12, according to [13].

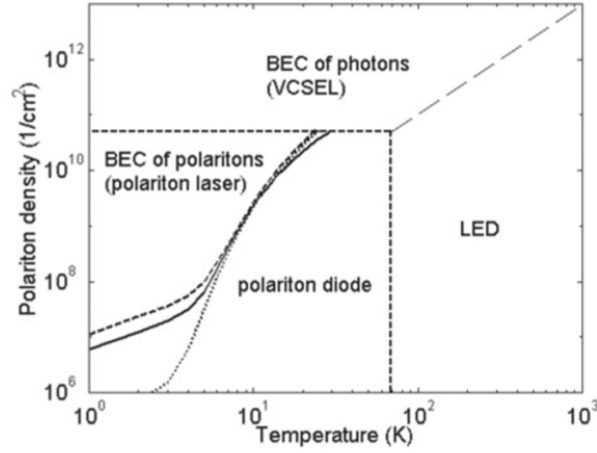


Figure 2.12. Phase diagram of polariton condensates in GaAs system

The perpendicular and horizontal dashed lines mark the boundaries of the strong coupling. The solid lines describe the critical density  $N_c$  in respect to phase transition temperature for  $k_B T$ . The Dashed lines on either side of the solid line represent the critical density  $N_c$  for semi-condensation in systems measuring  $100\mu\text{m}$  and  $1\text{m}$  respectively. [13]

### 2.5.2 Polariton lasing

As seen in section 2.5.1, polaritons easily form condensates similar to Bose-Einstein condensates. Polariton condensates residing in the strong coupling regime, emit coherent light. Vertical-cavity surface-emitting laser (VCSEL) structures also emit coherent light from QWs placed inside a microcavity. Despite the similarities, we say that VCSELs emit photon laser while polariton condensates emit polariton laser. The main difference between polariton lasing and photon lasing is that the latter operates through the population inversion principle while polariton lasing does not. Specifically, photon lasing operates under the weak coupling regime through stimulated emission. In that case, an electromagnetic field is the only thing that plays a part in amplification due to the positive feedback of the cavity. Photons do not interact with each other.

In contrast, polaritons are a mixed state between polaritons and excitons in QWs. As a result of the strong coupling of light and matter, polaritons share properties from photons and excitons accordingly. Polaritons, partly created by bosons, inherit some of their properties such as the particularly small effective mass leading to relatively high temperatures and low density in which bosonic degeneration occur. At the same time, interactions in the polariton gas are introduced by exciton wave-function component. These interactions are the main difference between polariton and photon laser. Moreover, the strength of the interactions can be modulated from changing the detuning, in turn changing the balance between photonic and excitonic behavior.

For a polaritonic system, the pump excites carriers which form the exciton reservoir of the system. Polariton-exciton, polariton-polariton and exciton-phonon interaction cause the scattering of excitons into polariton states. The linewidth of polariton increases with larger excitation power. Verifying the previously mentioned interactions [19]. For low pump power, polariton density and emission is linearly related to pump power. Polaritons relax from high values of momentum and start to accumulate to the same energy state at  $k_{||}=0$ .

Exceeding the condensation threshold, one can observe macroscopic phase coherence. Increase of the coherence period corresponds with reduction of linewidth. The above remarks show that interactions due to exciton mode, contribute to notable variances between polariton and photon laser. Another key difference is the natural origin of coherent emission in both systems. In the case of polariton laser, coherent emission begins when the occupation of the fundamental state is greater than one. In turn, the previous takes place when the rate of the population occupation is greater than the emission rate. Under these circumstances, the energy relaxation to the ground state becomes stimulated (bosonic final state stimulation). However, the emission from the condensate, through photonic leakage from the microcavity is still spontaneous, and is given by the lifetime of polaritons. Thus, the inversion condition is not necessary for polariton laser. The concentration always occurs for the same total carrier density in the system assuming that the polariton-exciton scattering rate exceeds the radiant losses. This behavior is in stark contrast to those observed in VCSELs, which operate in the weak coupling regime. In VCSELs, the laser action is due to the reconnection of the electron-hole plasma at the active material. Figure 2.13 depicts an energy dispersion schematic comparing photon and polariton condensate laser while figure 2.14 compares the two regimes with respect to carrier density.

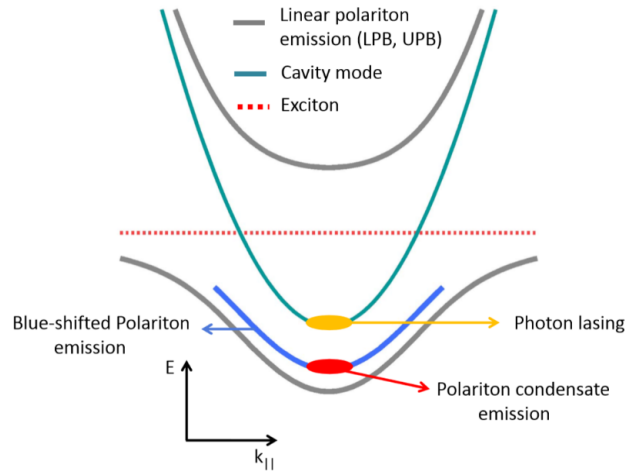


Figure 2.13. Qualitative energy dispersions comparing polariton condensate and photon laser

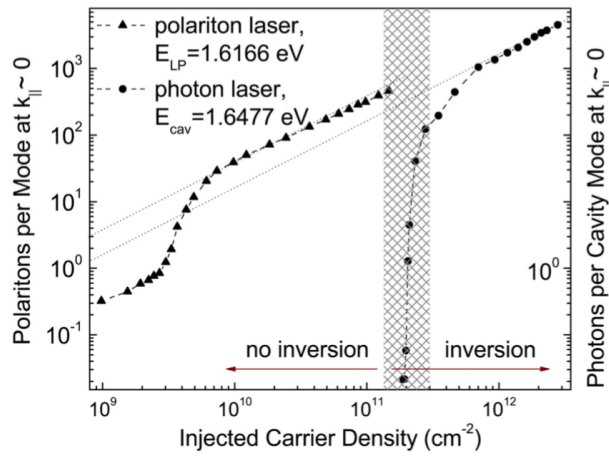


Figure 2.14. Polariton and photon density per mode with respect to injected carrier density.

### 2.5.3 Blueshift and polariton trapping

Bose-Einstein condensates exhibit a property of a quantum fluid called *superfluidity*. They are considered to be fluids with zero viscosity and zero scattering while propagating under a critical velocity. This property has been observed in Helium-4 and Helium-3 isotopes, winning the 1996 Nobel prize [20]. This behaviour is also later observed in ultracold atoms [21] and even in neutron stars as proposed by [22]. Polariton

condensates closely resemble Bose-Einstein condensates minimal polariton-polariton interactions, a key requirement for superfluidity [23]. Since polariton condensates, opposed to other systems, survive temperatures up to room, they are, to my knowledge, the only system that offers the ability to study superfluidity in such high temperatures. With this in mind, there is no surprise that polariton condensates can travel along one point to another like a wave packet [24].

### 2.5.3.1 Potential landscape

The potential energy landscape of the microcavity sample is not flat. Either intrinsic disorders of the sample either engineered disorders such as waveguides, detuning gradients and micro-pillars can create arbitrary potential landscapes. The potential landscape of the sample also alters simply by the electromagnetic field of the pump beam: due to the large local density of excitons generated around the excitation spot, exciton-exciton and polariton-exciton interactions generate a local potential peak called the *blueshift potential* (figure 2.15).

$$E_{blueshift} = gn_{pol} + \tilde{g}n_r$$

where  $\tilde{g}$  represents the exciton-exciton interaction and  $g$  the polariton-polariton interaction. Under non-resonant excitation (meaning the wavelength of the excitation beam is larger than the resonance of the QW, located on another minimum of the reflectivity spectrum of the microcavity), with the laser spot measuring about  $1\mu\text{m}$  on the sample surface, an electron-hole plasma is generated which rapidly relaxes to form the excitonic reservoir of the system. Excitons couple with the cavity mode generating polaritons with large kinetic energy (momentum,  $k_{||}$ ). Polaritons relax to lower  $k_{||}$  values and through bosonic final states. Though bosonic final state stimulation [25], polariton relaxation rate to the lowest energy state is proportional to the density of polaritons to the same state and they form condensates. Due the exciton density being comparable with Mott density, the fermionic character of excitons starts to play an important role. Exciton-exciton and polariton-polariton interactions give rise to the aforementioned blueshift potential. The polariton condensate, generated on the peak of the potential, accelerates radially and ballistically, converting the potential energy to kinetic energy, 'seeking' a local potential minimum. The kinetic energy of the condensate resulting from potential energy [24] is given by :

$$k_{||} = \frac{\sqrt{2m^*E_{bshift}}}{\hbar}$$

Owing to their small effective mass and high mobility, they diffuse at distances greater than  $100\mu\text{m}$  before finally escaping the MC as photons. Excitons on the other hand, since their effective mass is considerably higher and their mobility much lower than that of polaritons, diffuse at shorter distance around the excitation spot ( $\approx 4\mu\text{m}$ ).

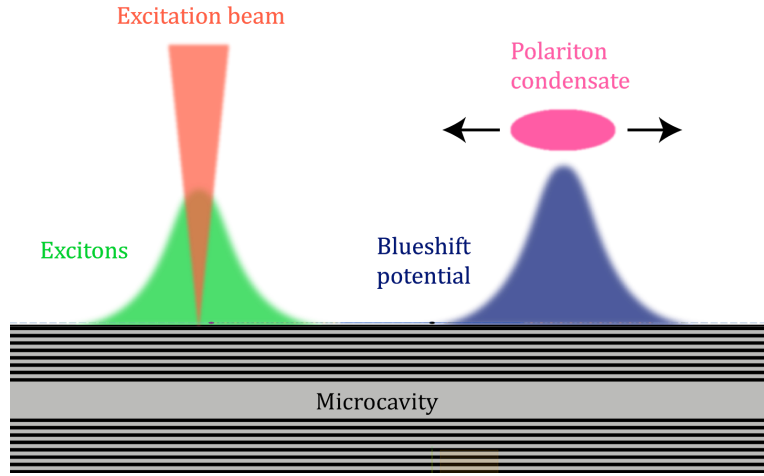


Figure 2.15. Schematic representation of the generation of blueshift potential. Left: The pump beam (orange) is focused onto the microcavity sample generating a local increase of exciton density (green). Right: Increase of exciton density results in exciton-exciton interactions, locally increasing the potential energy (blueshift potential, blue). Polariton condensate is realized at the peak of the blueshift potential. Since they are located to a local maximum of potential energy, they propagate ballistically and radially, by converting the potential energy to kinetic energy.

The diffusion distance is given by:

$$D = \frac{\mu k_B T}{e} \quad \text{with} \quad \mu = \frac{e \tau_{sca}}{m^*}$$

where  $\tau_{sca}$  is the scattering time. Using the potential landscapes, we are able to manipulate the kinetic energy and spatial distribution of polariton condensates. Polariton waveguides have been used successfully achieving propagation of polariton condensates for long distances [26][27]. Optical patterns are used to create polaritonic traps and lattices [28][29].



### 2.5.3.2 Trapped polariton condensates

Trapped polariton condensates pose several advantages over their free propagating ones. The most important advantage is the ability to study the polariton condensates delocalised from the exciton pumps. This creates the conditions for unobtrusive imaging. Trapped polariton condensates also exhibit reduced blueshift, have narrower linewidths and they are less affected by the spin noise of the exciton reservoir. Figure 2.16 schematically represents the potential landscape of a trapped polariton condensate.

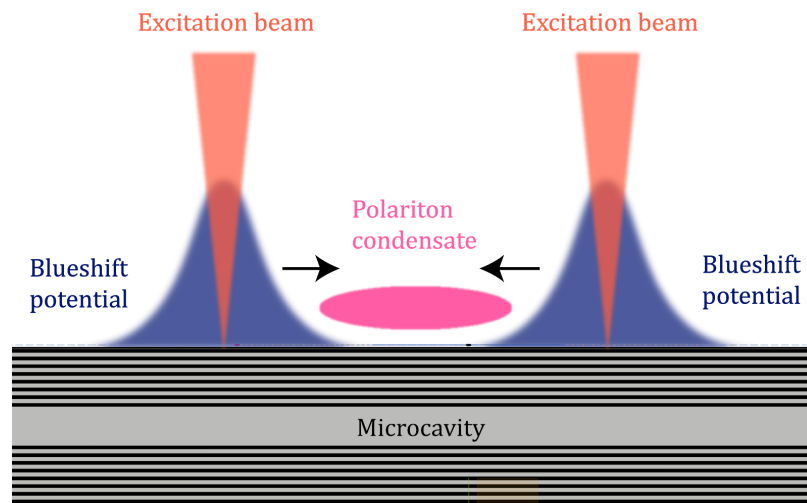


Figure 2.16. Schematic representation of the potential landscape of a trapped polariton condensate. The spatially modulated excitation beam is focused in two spots on the sample, locally generating blueshift potentials. In the middle of the excitation pattern, a local minimum is generated, trapping the condensate.

The spatial intensity modulation of the excitation laser as a technique to generate arbitrary potential landscapes is in some ways advantageous compared to direct manipulation of the sample structure. The first obvious reason is the versatility of this technique: any arbitrary excitation pattern can be projected to the sample; a feature ideal for experimentation for spot diameter, shape and distance. Moreover, using this technique it is possible to address the height of each blueshift potential individually. This allows the generation of small potentials by locally reducing the incident power below lasing threshold. These potentials act as barriers, allowing the manipulation of the coupling strength between two neighbouring condensations [30]. In section 3.3 there will be an in-depth explanation of the technologies and experimental setups used for the pumping procedures.

### 2.5.4 Spin of polaritons

An electromagnetic wave with its electric field continuously rotating around the axis of propagation is said to be circularly polarized. The circular polarization can be either left or right handed. Photons of circularly polarized light entering the microcavity, carry Spin Angular Momentum (SAM). For elliptical and circular polarization, SAM is non zero while for linear polarization, it is zero. In the quantum description of light, SAM is an observable with its corresponding operator:

$$\vec{S} = \sum_k \hbar u_k \left( \hat{a}_{k,L}^\dagger \hat{a}_{k,L} - \hat{a}_{k,R}^\dagger \hat{a}_{k,R} \right)$$

where  $k$  is the wavevector,  $u_k$  is the propagation unit vector, pointers L and R refer to the handedness of the states  $|L\rangle$  and  $|R\rangle$  respectively. For circularly polarized light, a single photon's eigenvalues are either

$$|L\rangle = \frac{1}{\sqrt{2}} \begin{pmatrix} 1 \\ i \end{pmatrix} \quad \text{or} \quad |R\rangle = \frac{1}{\sqrt{2}} \begin{pmatrix} 1 \\ -i \end{pmatrix}$$

and the spin projection on the axis of propagation is  $S_z^{ph} = \pm 1$ . For this thesis, the projection will be referred to as  $\sigma^\pm$ .

Excitons have spin projection to the growth axis of either  $S_z^X = \pm 1$  or  $S_z^X = \pm 2$ . The SAM of photons is distributed to the excitons through conservation of angular momentum. Excitons with projections  $\pm 1$  will be excited [31] by the incident photons, while those with projection  $\pm 2$  will not interact with inbound photons and will constitute the *dark states* [32] while interacting excitons constitute the *bright states*. During radiative relaxation of the bright excitons, the conservation of angular momentum dictates that the emitted photon should exhibit circular polarization. The polarization of polariton is expressed [33] as:

$$\rho_k = N_k \left[ \frac{I}{2} + S_k^{ph} \cdot \sigma_k \right]$$

were  $k$  is the observation direction,  $I$  is the identity matrix and  $\sigma_k$  is the Pauli matrix that corresponds to the observable in the chosen  $k$  direction. The pseudospin vector  $S_k^{ph}$  represents either the in plane component of the spin (dipole moment orientation) or the component perpendicular to the plane (spin). A convenient way of representing the polarization state of an electromagnetic field is using the Stokes vectors. Stokes vectors [34] are a set of 7 4D vectors that their combination represent any state of polarization. These vectors can be mapped to a unity sphere called the *Poincare sphere* figure 2.17.

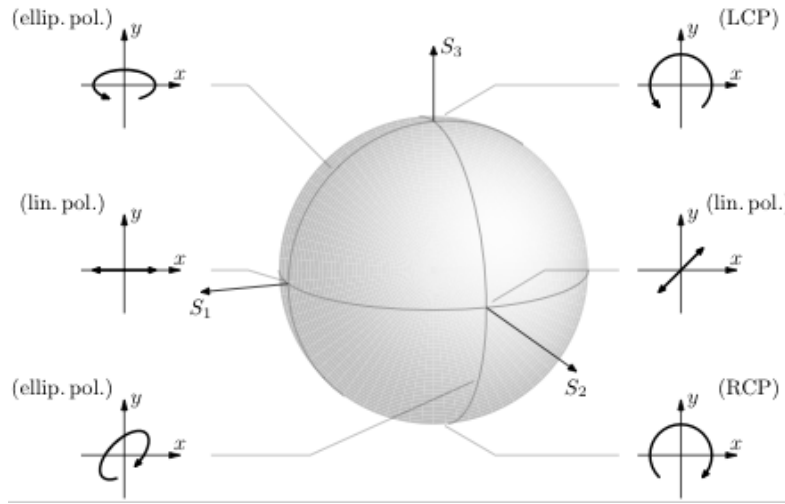


Figure 2.17. Poincare sphere mapping the seven Stokes vectors (the seventh represents unpolarized light and it is mapped at the origin of the axis)

The Stokes parameters  $S_{sto_k}$  can be measured as:

$$S_{sto_x} = \frac{I_H - I_V}{I_H + I_V}, \quad S_{sto_y} = \frac{I_D - I_{AD}}{I_D + I_{AD}}, \quad S_{sto_z} = \frac{I_{\sigma^+} - I_{\sigma^-}}{I_{\sigma^+} + I_{\sigma^-}}$$

were  $I$  is the measured light intensity. The pointers  $H, V, D, AD, \sigma^+, \sigma^-$  represent horizontally, vertically, diagonally, along the antidiagonal polarized light and right handed, left handed circularly polarized light respectively. Chapter 4 of this thesis will mention the experimental findings of temperature dependence of the *degree of polarization*. This refers to  $S_{sto_z}$ .

## 3 Experimental procedures

### 3.1 Introduction

This chapter explains the various experimental techniques used in order to measure the spin polarization of trapped polariton condensates with respect to temperature.

### 3.2 Trapped polariton spin: state of the art

Spinor polariton condensates are being very actively studied as they are proving to be excellent candidates for systems used for quantum simulators, Ising spin models, random number generators, q-bits etc. For the better understanding recent advances on this relatively new field, the following section presents some recent studies that are closely related to the subject of this thesis.

Spatially trapped polariton condensates have been observed to exhibit parity breaking bifurcation. [30] , using a membrane microcavity, Ohadi et. al. show that under non resonant excitation and at a critical density, the polariton condensate magnetizes spontaneously adopting randomly one of two elliptically polarized states, emitting either left or right handedness circularly polarized light with a degree of polarization up to 95%. They find that the magnetization of the condensation remain stable for long time scale (seconds) at low temperatures (5K) but starts flipping in higher temperatures. With the pump beam set to more than 10% elliptical polarization (either left or right handed) they measure that the polariton condensate deterministically emits the corresponding circular polarization. This is possible as polariton condensates are spatially separated from the pump spots and thus dramatically reducing interactions of polaritons with the unpolarized exciton reservoir. Finally they proposed that thermal noise is responsible for the increase of polarization flip frequency above 15 Kelvin.

Moreover, strong linear to circular polarization conversion is observed [35] by tuning the angle of linear polarization in polariton condensates trapped in a ring excitation pattern. A small ellipticity of the pump is induced due to the tight focus of the electromagnetic field[36]. Above threshold, density dependent bosonic amplification favours the polariton spin with the higher occupation. By spatially separating the polariton condensate from the reservoir, interactions with particles in the reservoir are suppressed and thus spin decoherence is reduced [29]. Spin reversal is observed to be dependant of optical

excitation densities. This is explained by the balance between internal Josephson coupling effect and the detuning of two projections of the spinor condensate by transitioning from synchronized to desynchronizes regime. This observation opens the way to the use of such systems as optical switches.

To use polaritonic devices as optical switches by exploiting their spin properties could be beneficial as such systems offer lower energy consumption [37] and better signal transfer compared to their electronic counterparts. Polariton spins can be manipulated optically[38][39] or by strong magnetic fields[40][41]. [42] propose an electrooptical polariton switch by using external electric field to control the spin of polariton condensate with ultra low switching energies, opening the application of such a device to be assembled on a chip.

Another study[43] shows how spinor polariton systems can be interact with first neighbours systems by realizing two trapped polariton condensates next to each other, separated by a blueshift barrier. Coupling between the two condensates is due to Josephson tunneling. They control the coupling by lowering the barrier between the two condensates or by increasing their spatial distance. The excitation beam is linearly polarized resulting in the stochastic polarization of the condensations. Depending on the coupling strength, there are either ferromagnetic or antiferromagnetic configurations. With lower barrier, the coupled polariton condensates exhibit ferromagnetic configuration while with larger barrier they switch to antiferromagnetic. For an intermediate value, there is no correlation.

Expanding to the previous study, [44] demonstrate larger spinor polariton condensate systems with nearest neighbour controlled interactions. Their system is comprised of closed 4 condensate chains and 8 condensate chains. The condensates are generated by optical square lattices. By controlling the barriers between the condensations and thus the Josephson coupling, the system transitions from ferromagnetic to anti-ferromagnetic phase. Depending on the dialed interactions, (intensities of the corresponding excitation spots) the 2x2 condensation lattice can be configured to eight states: Two ferromagnetic, four paired ferromagnetic and two anti-ferromagnetic. The paired ferromagnetic configurations lead to the conclusion that the system is not governed by the minimization of free energy opposing to the standard equilibrium Ising spin model. For the larger eight condensation chain, the microcavity inhomogeneity poses a problem constituting scaling to be not trivial. Closed loop feedback algorithms help overcome this problem by compensating for the aforementioned inhomogeneity. They observe Without the compensation, the system behaves like a 'spin glass' with random interactions between neighbours.

In order to better understand the parameters that control the spin flip rate, [45] study the effect of pump power. The excitation pattern comprised of four spots that make an optical trap. The pump is non resonant and linearly polarized. They find that flip rate is not

linearly dependent on the pump power. They find that at powers near the bifurcation limit, since the magnitude of the spin is small, spin noise from the nearby reservoir is very probable to have amplitude larger than the condensation spin and thus flipping it. Increasing the power the average flip rate rapidly decreases as the magnitude of the spin (degree of polarization) is increased. Increasing pump power even more, the degree of polarization reduces and the average flip rate increases. Fast The average spin flip rate ranges four orders of magnitude for this experiment. The fastest flip rates are measured with single shot streak imaging and they are in the range of GHz. The very fast flipping of polariton condensate spin is key to considering such systems for use as Random Number Generators (RNGs) that compete with the state of the art [46]. On top of that, several uncoupled clones of the condensation can be easily used to create many RNGs working in parallel.

Spinor polariton condensates show optical bistability as described by [47]. Optical bistability is crucial for the formation of optical transistors and memory elements as well as 'digital' devices in general such as RNGs. They show that the overlap of the exciton reservoir with the condensate plays a detrimental role to the bistability while the hysteresis area of the degree of polarization versus the pump power can be controlled by pump geometry. The spatial profile of the condensate always occupy the lowest energy mode in the trap and has no effect on polarization flips.

The above studies are focused on exploring spinor polariton condensate systems for use in quantum computers and quantum simulators. They prove to be promising candidates for forming tool to study basic scientific fields such as condensed matter phenomena. They also seem to be usable in real world applications, filling in the gap that traditional methods leave behind due to their inherent limitations. In pursuit of quantum supremacy, basic research is needed in order to understand the parameters that control systems like polariton condensates. Moreover, applying the acquired knowledge to form useful devices that tackle unsolved or difficult problems is another exciting problem in itself. Engineering and basic science are combined in order to create tools for engineering and basic science.

More specifically, some of the studied input parameters and their corresponding mode of affecting the system are:

The microcavity sample which is the device responsible for strong light-matter coupling and hence the creation of polariton condensates. It dictates the detuning from QWs, the Q factor (emission linewidth/emission wavelength), the resonant wavelength, operating temperature etc. The MC can be semiconductor, hybrid organic-semiconductor or hybrid inorganic -semiconductor and it can be either on a substrate or in membrane form.

Wavelength of the excitation beam determines if the excitation is resonant (at the same wavelength as the QWs emission) or non resonant (where the excitation beam has a wavelength lower than the QWs and is usually tuned to a minimum of the MC reflectivity curve). Non resonant excitation is usually preferred as the pump can be easily filtered for easier detection of the condensate emission, without the pump scatter. In addition, the MC samples (due to molecular beam epitaxy manufacturing) usually feature a gradient in detunings. This limitation is usually helpful for experiments since it allows the precise control of the cavity modes wavelength.

Pump power density is responsible for many effects regarding spinor polariton condensates. It determines the exciton density and thus the blueshift magnitude. It is also one of the factors in controlling the spin flip rate. Moreover, with linear excitation, power is a key factor for controlling the spin flip rate. With circularly polarized excitation, the power of the pump has an effect on the degree of polarization of polariton condensates. Power also determines if the polariton condensate is below or above the lasing threshold and hence its linewidth.

The pumps spatial and phase profiles are responsible for generating optical traps by taking advantage of the blueshift potential. Flexible and easy to make arbitrary patterns can be induced in the form of this energy potential. This allows the creation of Hamiltonian simulations, lattices, controllable potential heights that in turn control the coupling strength of nearby polariton condensates. These interactions can be used to create Ising spin models with controlled first neighbour interactions. Ising spin models have been proven to be able to solve complex optimization problems.

One more mode of control is the polarization of the excitation beam. Even with linearly polarized pump the spin of polariton condensate emits circularly polarized light with a high degree of polarization. In this case, the spin of polariton condensates is determined randomly by amplifying the small ellipticity of the pump caused by the projection optics or irregularities of the MC sample. With circularly polarized excitation beam, polariton condensates (in most cases) inherit-through conservation of angular momentum-the spin that correspond to the emission of circular polarization with the same handedness. Spin information is easily accessible by simple polarimeter setups.

The potential of spinor polariton condensates as an easy controllable and versatile system is shown by the growth of interest in this field by the scientific community. Further study of such systems and their use in industry is in part hindered by the cryogenic temperatures that favour the formation of polaritonic condensation. High end even room temperature polariton condensates have already been observed by []. To my knowledge,

there are no studies focused on the effect of temperature on spin of polariton condensates. In this study we intend to fill this gap. Temperature dependence is important (in my opinion) not only for economical reasons but as of general interest of the mechanisms that take place and affect the system. Never produced before data points on the effect of temperature to the spin of polariton condensates can lead to a more accurate understanding of the system. In addition, understanding the mechanisms that lead to loss of degree of polarization and increased spin flip rate with increasing temperature could lead to the suppression of non-desired effect and thus more usable commercial spinor polariton condensate systems. In the following experiment we depart from cryogenic temperatures, reaching near room temperature 250K while we observe degree of polarization  $> 87\%$  at 100K with CW excitation.



### 3.3 Experimental setup

This section introduces the various experimental setups developed for the study of polariton condensates. Specifically, the experiments performed are real-space and k-space one shot spectroscopy for sample with the addition of polarimetry for spin measurements. Finally a fast-response polarimetry setup is developed for studying the dynamics of the spin of polariton condensates and the effect of temperature on it.

#### 3.3.1 Photoluminescence

As mentioned in section 2.3.2, the in plane momentum  $k_{||}$  is conserved in each layer according to Snell's law. As a result, a photon with in plane momentum  $k_{||}$  can be coupled only to an exciton state with the same  $k_{||}$ . The polaritons resulting from this coupling also have the same  $k_{||}$  and angular momentum as the corresponding input photon. Polaritons decay by 'releasing' photon out of the microcavity. This correspondence is responsible for the ability to gain information about polariton by measuring the 'escaped' (emitted) photons. Information about the energy of polaritons is also preserved. The wavelength of emitted photons is determined by the transition energy of the exciton state and it directly corresponds to the energy of polaritons. Finally, through conservation of angular momentum, the polarization of the emitted photons carries information about the spin of polaritons as mentioned in section 2.5.4: right-handed and left-handed circular polarization directly corresponds to spin +1 or -1. Information about energy  $E$ , spin  $S$  and momentum  $p = k_{||}\hbar$  is enough to reconstruct the state of polaritons. Moreover, the intensity of the emitted light provides information about polariton density. By recording the angle resolved (k-space) photoluminescence spectra, one can directly measure the full dispersion curve of polaritons from which a multitude of important parameters can be deducted such as effective mass, density of states, photon-to-exciton fraction, coupling strength, detuning.

The physical process of photon emission can be classified as *photoluminescence* (PL). It is the spontaneous emission of light from the relaxation of an optically excited state. The type, energy, and amplitude of the excitation beam is selected according to the semiconductor materials and the desired information. PL spectroscopy provides accurate information about optical transitions and thus energy states. Time resolved PL measurements also provide information on the carrier lifetime. Finally, the change in the PL intensity in relation to temperature provides information about the various

non-radiative processes triggered by the temperature change and affecting the optical performance of the semiconductor.

The typical components used to perform such measurements are: a light source, (typically a laser source) for the excitation, a focusing lens, the sample to be measured, a collection lens and a spectroscope. for this experiment, we use a variance of PL spectroscopy: the micro-PL spectroscopy, based on the same principle but combined with a microscope objective lens instead of the focusing and the collection lens. A filter is also preferably placed at the collection to eliminate the scattered pump light before it reaches the detector. Considering the direct relation between emission angle and momentum, combining micro-PL measurements with angle resolved imaging results in the ability to directly measure the dispersion curve of the polariton condensates. Figure 3.1 is a diagram of the experimental setup used for single-shot polariton dispersion imaging and single-shot energy resolved imaging.

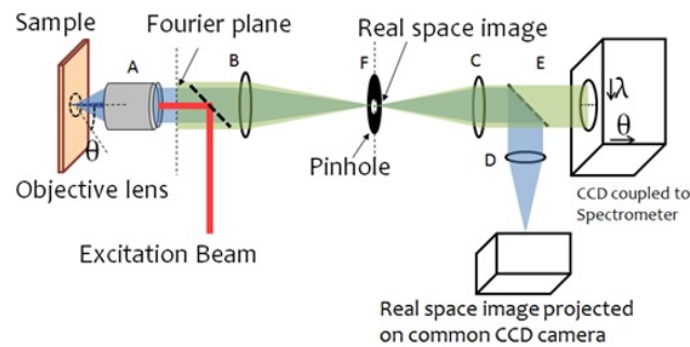


Figure 3.1. Angle resolved spectroscopy experimental setup.

### 3.3.2 Real space spectroscopy

For the excitation, a Ti:Sapphire continuous wave or pulsed laser source is used as the pump beam. The laser is tuned non-resonant 760nm. It is then spatially modulated by a Texas Instruments DLP evaluation board with its respective DMD chip. finally, lens images the surface the DMD chip. This produces a patterned beam. The excitation beam passes through a beam splitter to be redirected to a 50x microscope objective lens (A) placed at focal distance from the microcavity sample, the laser pattern is focused on the microcavity acting as the excitation beam. The microcavity sample is in turn is placed in a low vibration cryostat. Light emitted for the sample (blue beam) passes through the same objective lens

(A) and gets magnified. The real space emission beam is then split into two branches by a second beam splitter. One branch reaches a CCD coupled spectrometer paired with its input lens (C) while the other branch reaches a simple CCD sensor paired with its respective input lens (D). Lenses (C) and (D), in conjunction with the microscope objective, determine the final magnification of the respective optical path: for 50x magnification, (C) and (D) lenses should be of 200mm focal length.

### 3.3.3 K-space spectroscopy

For retrieving information about  $k_{||}$  we take advantage of the Fourier transform and inverse Fourier transform performed by the microscope objective lens. Any objective lens creates the diffraction pattern of the object in its back focal plane (otherwise called the Fourier plane) (figure 3.2). All light emitted for the microcavity with the same angle will be in the same point in space at the Fourier plane. The range of the collected angles (-30 degrees to 30 degrees) is determined from the numerical aperture of the microscope objective:  $NA = n \sin \theta = n \sin[\arctan(D/2f)]$ . Where  $D$  is the pupil diameter and  $f$

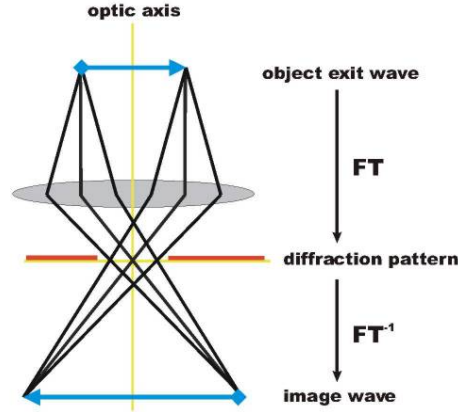


Figure 3.2. Fourier analysis (FT) and Fourier synthesis (inverse FT) as a result of light passing through an objective lens.

the focal length of the objective. By imaging the Fourier plane with an imaging lens (B) to a spectrometer (green beam), we obtain information about both the energy  $E = \hbar\omega$  and  $k_{||}$  simultaneously. The relation of the energy and the wavevector constitutes the dispersion curve of the polariton condensates. The lens that images the Fourier plane (B) will from now on be referred to as Fourier lens. In our case, it is a flipping lens, allowing to change the detection from k-space to real-space.

### 3.3.4 Microcavity sample

The microcavity sample is responsible for light matter coupling, making it one of the most important parts of the experiment. It is formed using molecular beam epitaxy, a technique suitable for the manufacturing of III-V semiconductors with unparalleled precision. The heterostructure is composed of alternating GaAs/ $\text{Al}_z\text{Ga}_{1-x}\text{As}$  semiconductors, taking advantage of the close lattice constant ( $\alpha_{\text{GaAs}} = 5.653 \text{ \AA}$  while  $\alpha_{\text{Al}_{0.25}\text{Ga}_{0.75}\text{As}} = 5.655 \text{ \AA}$  with  $x=0.25$ ) and the large band gap difference ( $E_g^{\text{GaAs}} = 1.519 \text{ eV}$  and  $E_g^{\text{AlAs}} = 3.16 \text{ eV}$ ) to fabricate a sample with low count of impurities and easily engineered band structure. In order to obtain high Q-factor it is necessary to stack many periods of alternating GaAs/ $\text{Al}_{0.3}\text{Ga}_{0.7}\text{As}$  since they have similar refractive indices ( $n_{\text{GaAs}} = 3.71$  while  $n_{\text{Al}_{0.3}\text{Ga}_{0.7}\text{As}} = 3.468$ ).

The high Q-factor (310000) microcavity sample used for all experiments in this thesis is specialized in the observation of high temperature trapped polariton condensates. It features two DBRs with 50 pair layers of alternating  $\text{Al}_{0.15}\text{Ga}_{0.85}\text{As}$ /GaAs each. The cavity consists of  $\text{Al}_{0.3}\text{Ga}_{0.7}\text{As}$  semiconductor with optical length of  $5\lambda_0/2$ . Four sets of three 12nm GaAs/ $\text{Al}_{0.3}\text{Ga}_{0.7}\text{As}$  quantum wells are placed at the antinodes of the electric field (figure 3.3).

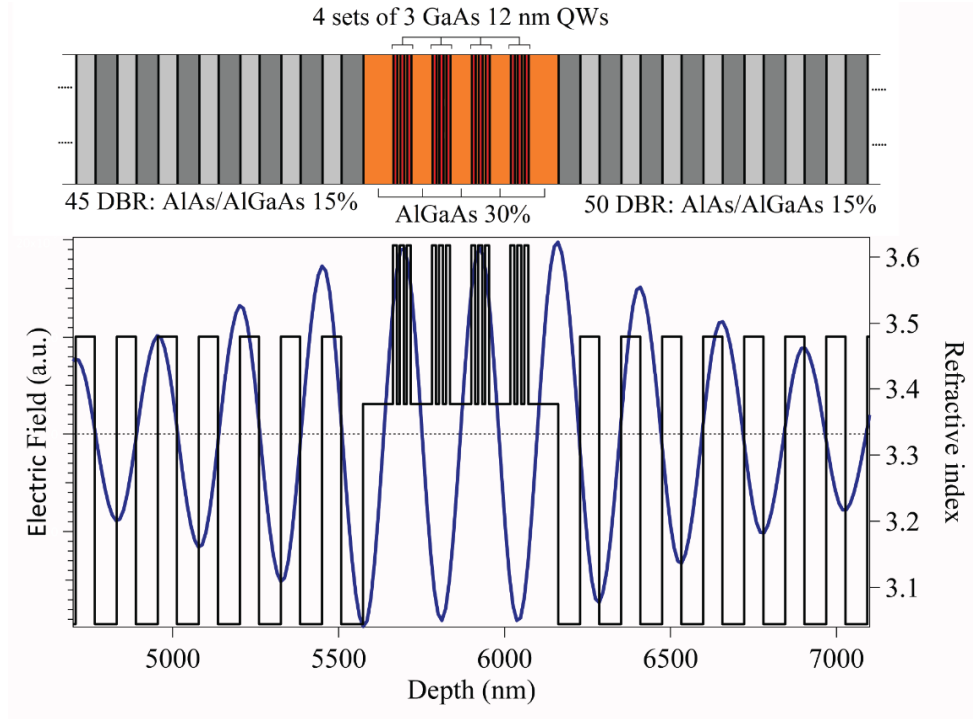


Figure 3.3. Microcavity structure and relative electric field intensity

The sample features wide detuning range for being able to sustain trapped polariton condensates at room temperature. A wide range of detunings is a necessity when working

at elevated temperatures since the energy level of exciton falls with rising temperature. More negative detunings are needed in order for the exciton reservoir to be able to feed the LPB efficiently. For efficient feeding, the exciton energy level should be in proximity above the energy level of the LPB. The samples range of negative detunings is sufficient for efficiently sustaining trapped polariton condensates from cryogenic temperatures to room temperature. In addition, the high Q-factor of the cavity is responsible for increased photon lifetimes.

The range of detuning can be experimentally measured using the setup mentioned in section 3.3.3. The cavity and exciton dispersion curves are extracted using energy resolved k-space imaging. Some experimental measurements taken at 7K are shown in figure 3.4.

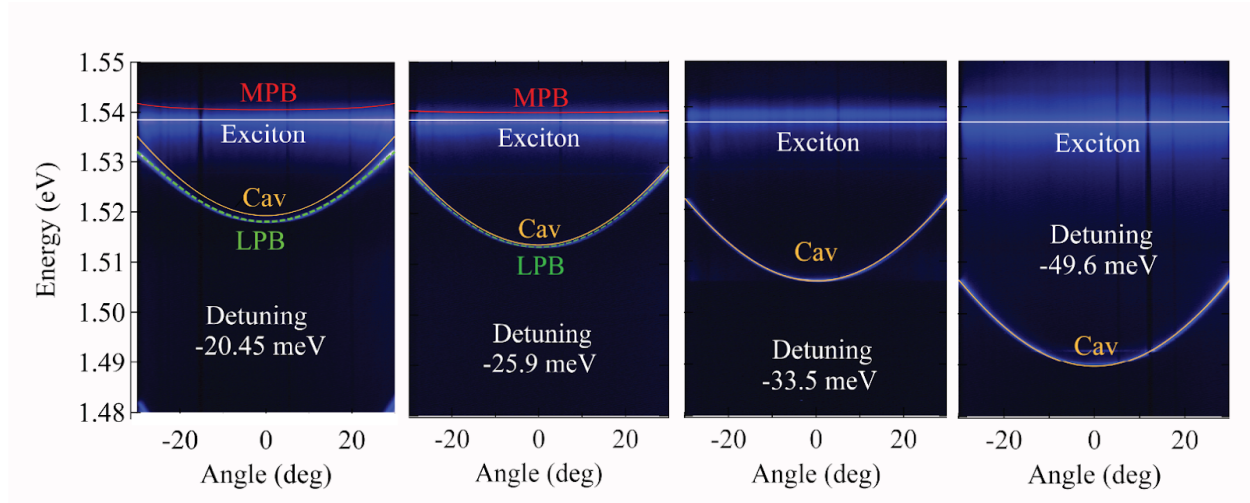


Figure 3.4. Dispersion measurements at different locations of the microcavity sample taken at 7K with excitation power below lasing threshold.

### 3.3.5 Arbitrary pattern generator

Invented by Texas Instruments, Digital Micromirror Device (DMD) technology (often marketed as Digital Light Processing (DLP) can be found in consumer projectors, 3D scanning and 3D printing devices. DMD devices are composed of an array of millions of very small ( $\sim 7\mu\text{m} \times 7\mu\text{m}$ ) pixel mirror elements. Each pixel is made of a multilayered device consisting of an aluminum mirror mounted on hinges along the diagonal. These pixels rest on a CMOS memory cell. By changing the value of the memory cell via a controller board, electrostatic forces alter the angle of the mounted mirror at 12 degrees in both directions. These mirrors can be repositioned rapidly at a rate of KHz. Each pixel is

individually addressable and it reflects light from a powerful Ti:Saph laser to an imaging lens or to a heatsink (light dump). In order to address the micromirrors, the user is expected to provide the controller board a binary image file with the same pixel count and aspect ratio as the DMD. Figure 3.5 the basic mechanism of the individually addressed micromirrors on the DMD chip.

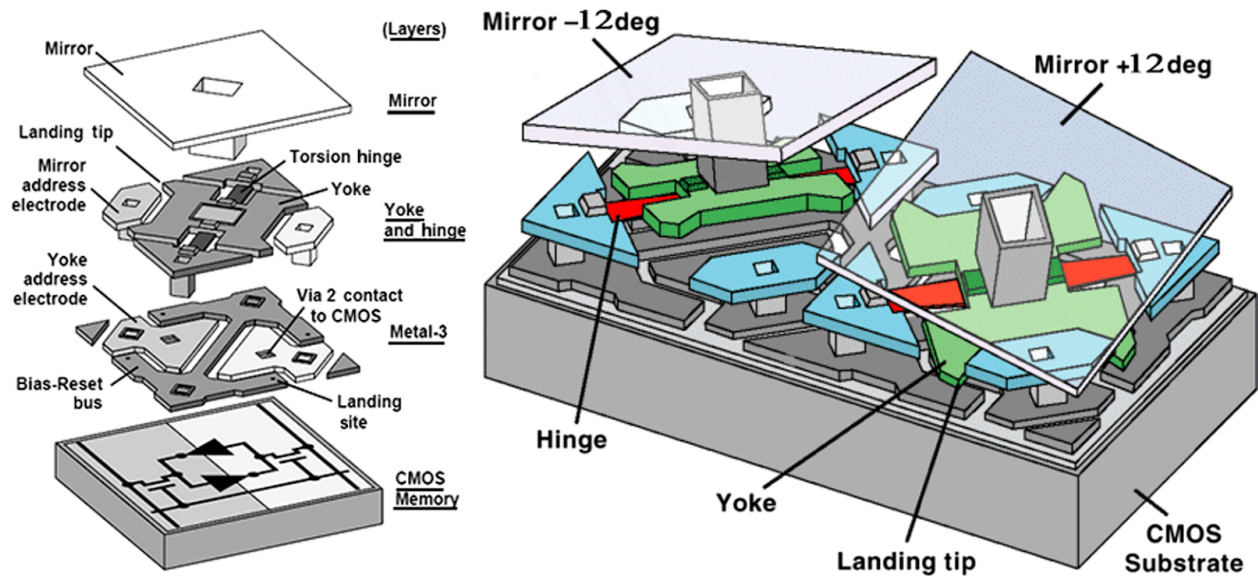


Figure 3.5. Operation diagram of a digital micromirror device (DMD).

As the DMD device allows only two states to each individual mirror ('On' or 'OFF'), the resulted pattern projected to the microcavity is monochromatic. Interesting effects emerge for polariton condensate lattices when the interactions between them are controllable. For controlling the blueshift barrier between polariton condensates, a new mode of control is needed: spatial intensity modulation of the pump pattern. In essence, we need to be able to project a grayscale image to the microcavity.

The DLP system is not designed to be used with semiconductor level response times. It is more frequently used for projectors, 3d scanning, printing and so on. With this in mind, by default, in order to achieve the illusion of analog control of the light intensity, the DMD mirrors flicker 'ON' and 'OFF' at a rate of Khz. The duty cycle of this squarewave flickering (Pulse Width Modulation) determines the perceived brightness for humans and other relatively slow processes such as photopolymerization in 3D printing. The time scale of semiconductor relaxation times is in the order of picoseconds. This renders PWM non



effective for modulating the intensity of the pump beam in order to control blueshift barrier height.

### 3.3.5.1 Error diffusion dither

Error Diffusion Dithering is a technique used to simulate tones of gray that are missing from low bit depth images. Using dithering, it is possible to map a grayscale image to a binary (single bit) image, which is the input of the DMD. The operating principle of dithering is that it maps the intensity (gray value) to the local density of 'ON' pixels; a white image contains 100% 'ON' pixel density (all pixels are white), a black image contains 0% 'ON' pixel density (all pixels are black) and 50% gray contains 50% 'ON' pixel density (half of the pixels are white and the rest are black). Figure 3.6 shows an 8-bit grayscale gradient and its conversion to 1-bit after applying dithering.

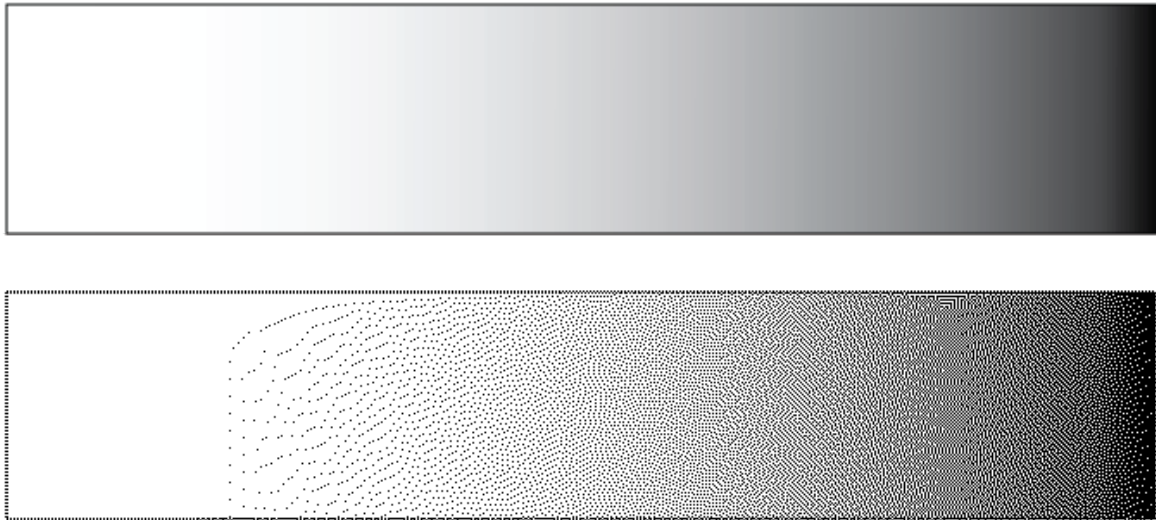


Figure 3.6. 8-bit grayscale gradient (top) and dithered grayscale gradient (bottom)

After dithering, the 1-bit image can be input to the DMD chip, ensuring that the mirrors do not flicker in order to create the illusion of variable intensity. Of course, a valid argument is that after imaging this sensor to the semiconductor, it now 'sees' several 'ON' and 'OFF' pixels as individual bright and dark spots as the resolution of the microscope objective lens is enough for projecting each individual pixel onto the microcavity. Here, resolution means the smallest detail that can be discerned as separate from the larger whole.

Conveniently, the Gaussian-like dissipation of excitons is larger than the average distance between two pixels.: with our setup, one pixel is projected to approximately 150nm on the sample while excitons diffuse to about 4 $\mu$ m from the excitation spot. This exciton behaviour act like a gaussian convolution filter, destroying high frequency information. Figure 3.7 is a simulation of how the excitons would 'blur' the projected dithered pattern onto the surface of the microcavity.



Figure3.7. Binary pattern representing an 8-bit grayscale gradient (up) and the same pattern passes through a Gaussian blur convolution filter representing the exciton density distribution (bottom) when the top image is projected onto the microcavity.

The bottom image in figure 3.7 resembles the original image in figure 3.6. Using exciton dissipation as representation of the pattern projected onto the microcavity is a valid strategy since the blueshift potential is determined mainly by exciton-exciton interactions.

### 3.3.6 Trapped polariton condensates

Trapped polariton condensates present various advantages over their untrapped counterparts. The main advantage of trapped polariton condensates is that they are spatially separated from their excitonic pumps. This separation leads to the reduction of the overlap and hence the reduction of exciton polariton interactions, resulting in the reduction of blueshift and linewidth. The uncoupling of polariton condensates from the excitonic pumps is due to the exciton having larger effective mass and thus exhibiting

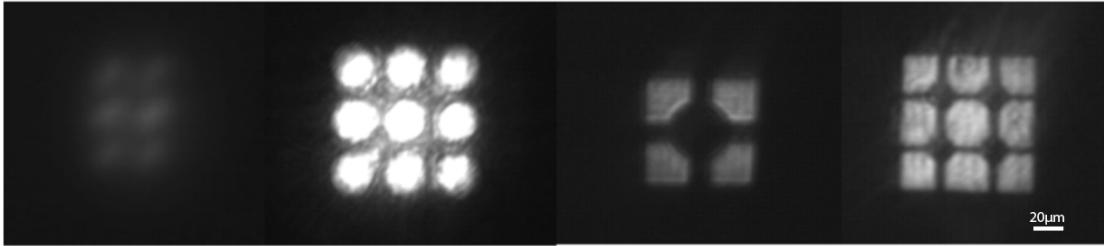


smaller diffusion lengths. In our case, the typical diameter of a trap sufficient to sustain a stable polariton condensate is  $10\mu\text{m}$ .

Since trapped polariton condensates do not overlap with the excitation spots and the exciton-polariton interactions are greatly suppressed, the weaker polariton-polariton interaction prevails, resulting in the reduced blueshift. Furthermore, the decoherence originated from hot excitons is also suppressed, leading to linewidth narrowing [48]. Delocalizing the condensate from the excitonic pumps also ensures low spin noise, making them ideal for spin resolved measurements.

Using multiple optical traps, we generate trapped polariton condensate chains and lattices. By manipulating the barrier between the nearest neighbours, we are able to control condensate-condensate interactions. The excitation geometry is an excellent source of control over polariton condensates. Figure 3.8 presents some patterns created by a DLP spatial light modulator, and the corresponding polariton condensates.

a. Excitation patterns projected on the microcavity sample



b. Polariton condensate emission

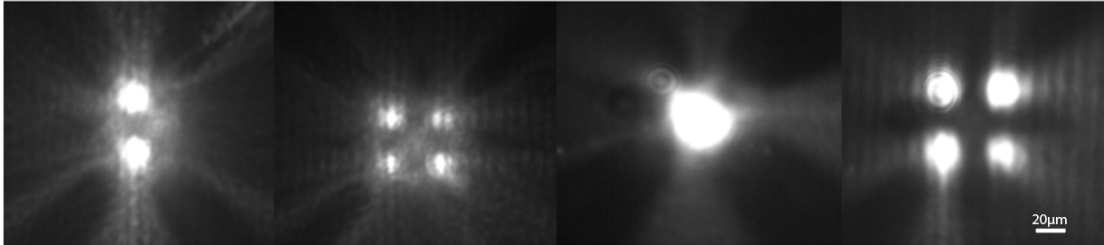


Figure 3.8. a: Example of patterns projected on the surface of the microcavity sample. b: polariton condensates generated from a.

### 3.3.7 Polarization resolved spectroscopy

This experiment is designed to measure the response of polariton spin with respect to temperature. Due to strong coupling between QW excitons and cavity photons, inherit properties from both. Thus, polariton spin is a result of direct coupling of exciton spin and photon polarization. Linear polarization in the excitation beam results on the condensate 'choosing' randomly spin=1 or spin=-1, resulting in the emission of either  $\sigma^+$  or  $\sigma^-$  polarized light. On the other hand, circular polarization on the excitation beam results mainly in polaritons with spin such that the emitted polarized light is circularly polarized with mostly the same handedness as the excitation beam.

#### 3.3.7.1 Excitation

A Ti:Sapphire laser is used as the pump. It is a continuous wave laser source tuned to a minimum of the macrocavity's reflectivity with higher energy than the resonance (760nm). The laser beam is spatially modulated by the DLP system to any arbitrary pattern. A lens is placed at a distance equal to its focal length from the DMD chip in order to image the plain of the DMD, where the pattern is formed. A linear polarizer ensures that the laser beam fully is horizontally polarised. A  $\lambda/4$  waveplate is used to convert horizontal polarization to elliptical polarization. Fully circular polarization is achieved with the fast axis of the quarter waveplate rotated  $\pm 45$  degrees from the axis of the linear polarizer; right handed to +45 degrees and left handed for -45 degrees. For 0 degrees of rotation we get horizontal, and for 90 degrees, vertical linear polarization.

A waveplate is a birefringent material meaning it has different refraction indices along two axis: the slow axis with larger refractive index and a fast axis with lower refractive index. It is used to alter the polarization of the light. The linearly polarized light entering the  $\lambda/4$  wave plate can be resolved into two waves; one parallel and one perpendicular to the optic axis of the wave plate. The component of the slow axis propagates slightly slower than the component of the slow axis. The result is that the component of the slow axis is delayed  $\lambda/4$  (or  $\pi/2$ ) exiting the waveplate. This causes the component wave to have a circular polarization as opposed to a linear polarization. If a circularly polarized light passes through a  $\lambda/4$  waveplate, it is converted to linearly polarized light accordingly.

The now patterned circularly polarized beam is projected on the microcavity sample after it passes through a beam splitter by an objective lens system with 50x magnification. With

this combination of lenses and actual size on the DMD, the patterns diameter is about  $10\mu\text{m}$ . The microcavity sample is placed inside a cryostat that features a precise temperature control system.

### 3.3.7.2 Collection

Light from the surface of the microcavity passes through the same objective lens and beam splitter. It consists of the substrate photolumination, the pump scatter and the polariton emission. Below lasing threshold, the only visible light is the substrate photoluminescence and the pump scatter. The pump scatter is the brightest component of the emission and it obscures the polaritonic detection. An interference long pass filter is placed after the beam splitter at the collection side in order to eliminate it. The emitted light is treated as having a polarization consisting of a linear combination of  $\sigma^+$  and  $\sigma^-$  circular polarization. Another  $\lambda/4$  waveplate is placed after the long pass filter for converting  $\sigma^+$  polarization to linear vertical polarization and  $\sigma^-$  to horizontal. Since light emitted from polariton condensates is a linear combination of  $\sigma^+$  and  $\sigma^-$  polarization, after the waveplate, the polarization is a mixture of vertical and horizontal polarization; in other words, linear diagonal polarization. The waveplate's fast axis is rotated 45 degrees from a polarizing beam splitter which separates the diagonal polarization into its vertical and horizontal components by splitting the beam into two beams: one vertically polarized and one horizontally polarized. The relative intensities of horizontal and vertical components directly correspond to the relative intensities of  $\sigma^+$  and  $\sigma^-$  components and thus the relative densities of polaritons with spin 1 and -1. Measuring the relative intensities of the perpendicular components, we extract the degree of polarization:

$$P = \frac{I_{\sigma^+} - I_{\sigma^-}}{I_{\sigma^+} + I_{\sigma^-}}$$

To measure the relative intensities, we use the CCD of the spectrometer for two reasons: The spectrometer spectrally isolates the emission of the condensate to that of the GaAs substrate, providing more accurate measurements. The second reason is that the spectroscope is equipped with a cooled high quality 16-bit CCD which dramatically improves the measurement's accuracy compared to other 8-bit sensors. 8-bit sensors can discriminate between  $2^8 = 256$  discrete levels of intensity while 16-bit sensors discriminate between  $2^{16} = 65536$  discrete levels of intensity. These amounts are called the *dynamic range* of a sensor. Light reaches the input of the spectroscope through an input lens (imaging lens 2) placed at a distance  $f$  from the horizontal slit. The two beams

are redirected to be close together and parallel to each other by two mirrors (M2 and M3) before they pass through a beam splitter (BS 2) as seen in the schematic diagram (figure 3.9). With opened slit, two real objects of the polariton condensate are projected on two different spots of the CCD sensor. The degree of polarization is deduced by measuring the count value for the pixels representing  $\sigma+$  and  $\sigma-$  polarizations separately.

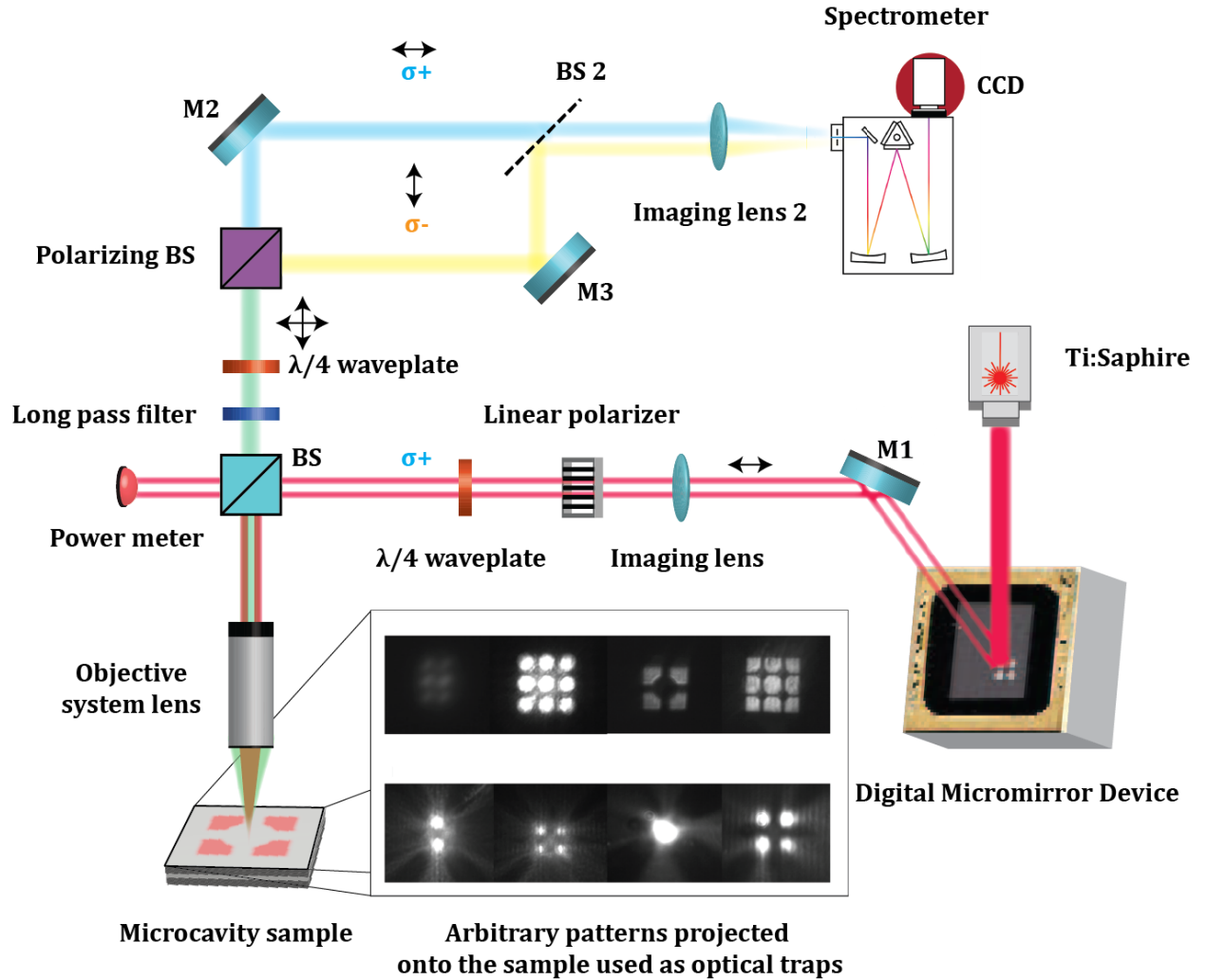


Figure 3.9. Schematic representation of the optical setup developed for spectrally resolved degree of polarization measurements.

### 3.3.7.3 Fast response setup

In the previous section we used the CCD sensor of the spectrometer to measure the average degree of polarization versus temperature. The limited sensitivity of the sensor, in

conjunction with the weak emission signal, the exposure times required for each measurement are in the order of tenths of seconds. Specifically, since the sensor is 16-bit, it has a dynamic range of 0 to 65535 of measured intensity for each pixel. This value determines the accuracy of the measurement. In order to achieve high accuracy, the measured intensity should be as close to the saturation values (but not above) as possible. For a specific quantum efficiency  $Q$  (meaning how many photons of a specific wavelength are needed in order to generate an electrical signal at a pixel) the measured intensity  $C$  in counts is:  $C = QT_{ex}I$  where  $T_{ex}$  is the exposure (integration) time and  $I$  is the intensity of the signal to be detected in watts per square meter. The measurement in counts is the result of counting the carriers generated from photons hitting the sensor over the exposure time for each pixel. Any event happening for the beginning of the measurement for the duration of the exposure time loses information about time. For example, a stationary light source that flashes with a period much smaller than the exposure time with 50% duty cycle would approximately produce the same number of photons as a non-flashing light source with half the intensity. A CCD camera that requires exposure time four orders of magnitude larger than the period of the flashing light would yield the same count measurement for both scenarios and no way to distinguish between them.

Although average degree of polarization is insightful, we would also like to study the dynamics of spinor polariton condensates in smaller timescales. Phenomena like spin flips, as they are analogous to a flashing light, are not detectable with the experimental setup of the previous subsection. The previous section revealed that with circularly polarized excitation, the degree of polarization drops with increasing temperature. The mechanism responsible for the loss of polarization is not yet clear. One scenario is that temperature introduces LO phonon spin noise to the system and increased spin noise from the dissociated excitons causing spin flips despite the circularly polarized excitation. Another scenario is that there are no spin flips and the intensity relation of  $\sigma^+$  and  $\sigma^-$  components changes with temperature again due to spin noise, resulting in the loss of polarization degree.

In order to study these effects, we need an experimental setup containing sensors with very fast response time which are very sensitive to light. A perfect candidate for this is a photosensor with photomultiplier tube (PMT) with half a nanosecond rise time, high dynamic range and typical maximum gain of  $3 \times 10^6$ . The principle of operation for these devices will be mentioned in subsection 3.3.7.4. Figure 3.10 depicts the optical setup developed using two of these sensors: one for each  $\sigma^+$  and  $\sigma^-$  component of the emitted light.

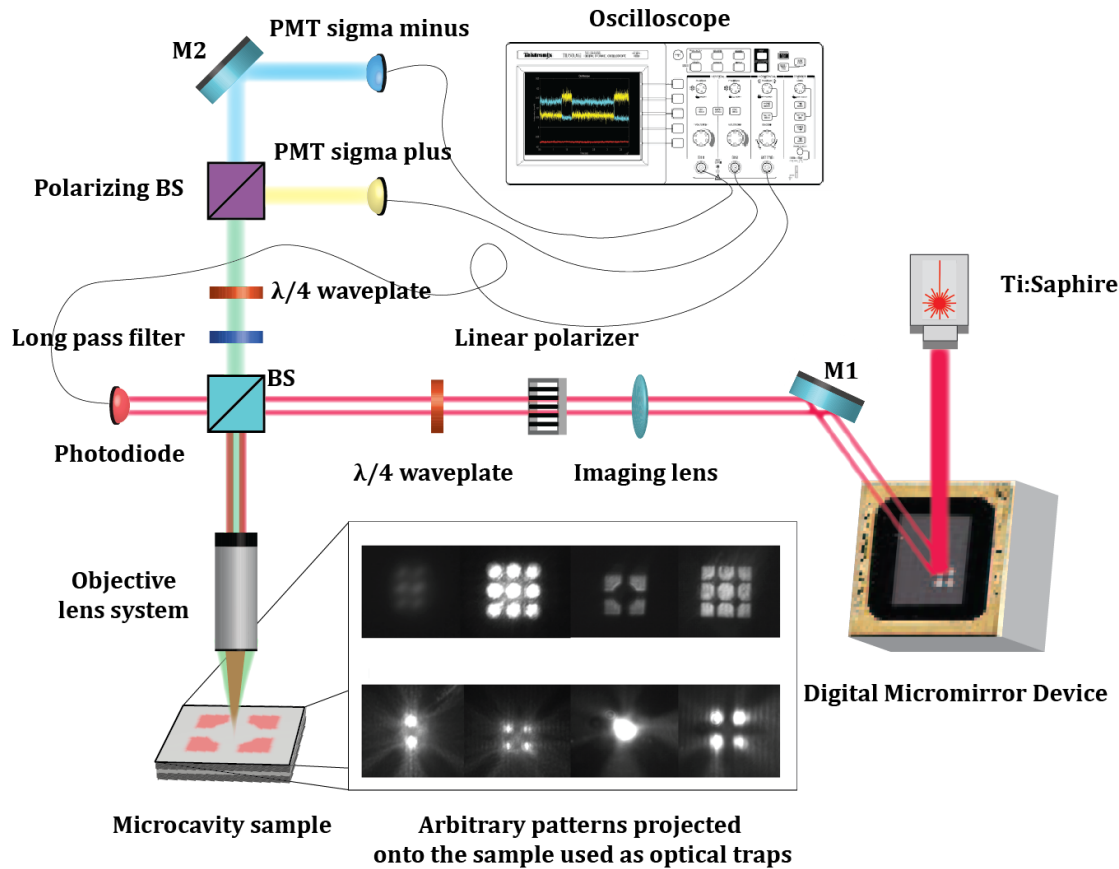


Figure 3.10. Time resolved polarimetry experimental setup.

For this experiment, the setup is largely unchanged from the previous one. The difference lies in the detection scheme. After the emission beam is split into two beams: one horizontally and one vertically polarized, they are individually directly detected by two separate PMT photosensors. The electrical signal produced by the photosensors is then measured over time by a high speed oscilloscope. Trigger for the oscilloscope is provided by a third channel whose signal is provided by a fast photodiode in place of the powermeter. This setup has the temporal resolution of about 50ns which is the response time of the PMTs. Each photosensors gain is determined by a control voltage. The fact that each photodiode has each own gain poses a problem compared to the previous setup: The gains must be as closely matched as possible as they determine the intensity values measured in order to extract the degree of polarization. This problem does not apply to the previous setup since there is only one sensor with the same gain value for all of its pixels. A gain calibration scheme is needed:

- The pump is set to fully  $\sigma^+$  polarization

- A neutral density filter is placed at the emission and the long pass filter is removed so that the pump scatter overwhelms the signal
- The channel of the oscilloscope corresponding to  $\sigma^+$  polarization( $s^+$ ) reads a value of  $S^+$  mV. The  $s^-$  channel should read values comparable to the amplitude of the background noise
- The pump is set to fully  $\sigma^-$  polarization
- The value on  $s^-$  channel:  $S^-$  should be the same value as the value measured from the  $s^+$  channel with  $\sigma^+$  polarization at the pump.

After this calibration scheme, the long pass filter is placed and the neutral density filter is removed. For verification, the pump is set to linear polarization resulting in spin flips. The measures spin flips are a good indication of the gain calibration. For circular polarized pump, after each measurement for example with  $\sigma^+$  polarization, another measurement is performed with  $\sigma^-$  polarization at the pump; the pair of measurements should yield opposite degrees of polarization. Note that degree of polarization  $P$  ranges from -1 to 1: -1 for 100% polarization with  $\sigma^-$  excitation and 1 for 100% polarization for  $\sigma^+$  excitation.

#### 3.3.7.4 PMT photosensors

PMT stands for PhotoMultiplier Tube . They are sensors specialized in the detection of faint signals. They feature large detection areas (compared to semiconductor counterparts), very high gain, low noise and relatively fast response. The principle of operation is: due to the photoelectric effect, input photons cause the generation of electrons at a cathode. Electrons are then accelerated by the electric field generated between the cathode and the anode. Several electron multiplying stages call dynodes are added in order to achieve high gain. Each electron colliding with a dynode generates secondary electrons according to the *secondary emission effect*. In the next stage, the secondary electrons together collide with the next dynode, producing many more and so on. Finally, the last stage electrons are collected through the anode. Each stage generates current amplification ranging from 10 to 100 times while there are typically about 15 stages. Figure 3.11 is a schematic representation of a modern PMT in a compact metal package, similar to the one used for this experiment.

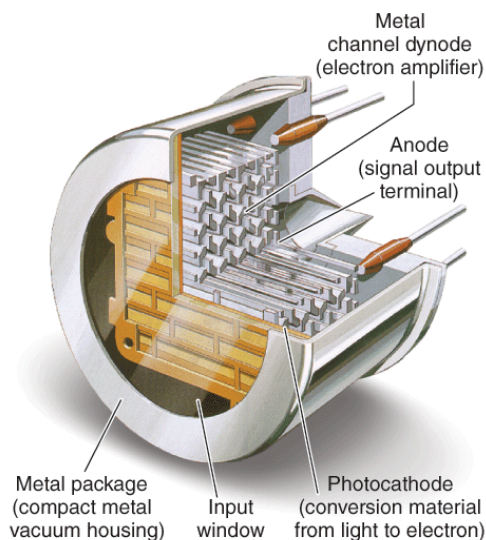


Figure 3.11. schematic representation of a modern PMT cross section in metal package.

## 4 Results

### 4.1 Temperature dependance on degree of polarization

This section is separated into two parts: The first part refers to energy resolved real space imaging using the CCD coupled spectroscop. The second part refers to time resolved measurements of the degree of polarization versus temperature and spin flips versus temperature using two PMT sensors.

#### 4.1.1 Spin resolved energy-real space imaging

The goal of this experiment is to record the maximum possible degree of polarization for the widest range of temperatures. The degree of polarization is in part determined by the polarization of the excitation beam. Since the system is bistable, for linearly polarized excitation, the condensate spontaneously and randomly adopts either  $\sigma^+$  or  $\sigma^-$  polarization due to any small spin imbalance caused by either temperature, the optics of tight focusing or sample impurities. For elliptical polarization at the excitation, the spin



imbalance is much larger resulting in condensate adoption polarization that matches the excitation. The maximum degree of polarization is achieved with circularly polarized excitation. This experiment is performed with  $\sigma^+$  excitation at 762nm. By raising the temperature, the energy of the exciton diminishes. To achieve maximum degree of polarization, different spots on the sample with different detunings are chosen.

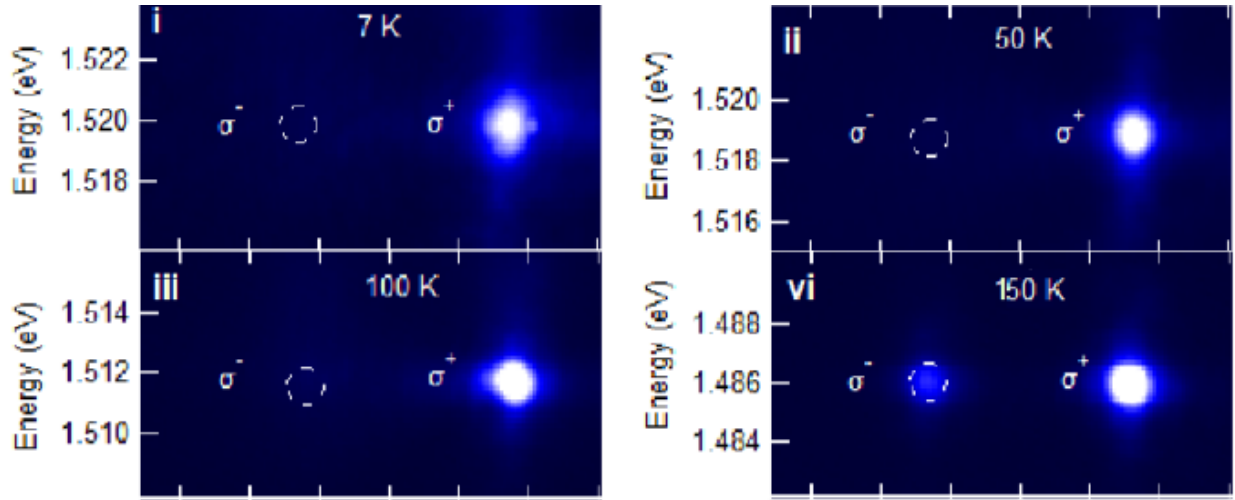


Figure 4.1. Spectrally resolved degree of polarization measurements.  $\sigma^-$  position is noted with dashed circles. Both  $\sigma^-$  and  $\sigma^+$  spots on the CCD are  $\sigma^-$  and  $\sigma^+$  polarized images of the same condensation

Sample measurements are shown in figure 4.1. High degree of polarization is observed for temperatures (above 50%) for temperatures up to 130K while for 150K the spin polarisation is 42% (figure 4.2). The pump power is about 1.5 times the threshold power, where the maximum polarization seem to occur. Note that the bright spots shown in figure 4.1, are only the polariton condensates as excitation pattern, visible through the substrate's photolumination is outside the spectrum range. Note that all experiments for this thesis are performed with trapped polariton condensates.

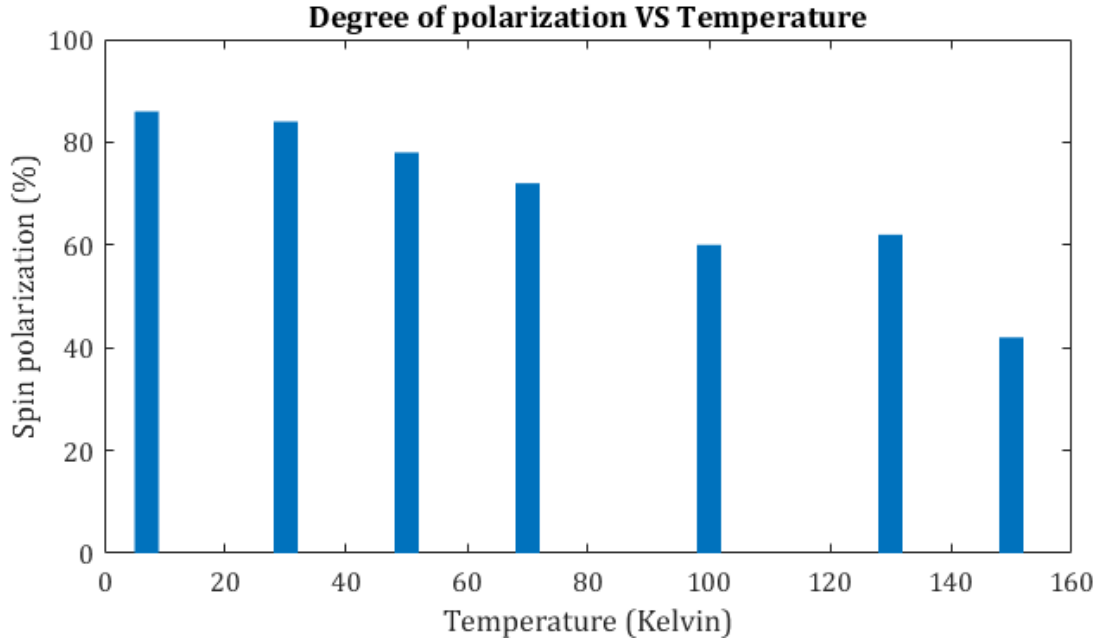


Figure 4.2. Extracted temperature dependence on the degree of polarization for  $\sigma^+$  excitation using relative intensities of a  $\sigma^+$  and a  $\sigma^-$  image of a trapped polariton condensate

The loss of degree of polarization with temperature seemingly is due to the loss of intensity in the  $\sigma^+$  component and gain of intensity in the  $\sigma^-$  component. The exposure times needed for the measurements are in the order of tenths to hundreds of seconds. Any possible spin flip occurring while the CCD shutter is open, could not be detectable. One mechanism for the loss of the degree of polarization is that the spin noise floor from the excitonic pumps gets large enough that it is able to temporarily flip the spin. Since the system is bistable, the spin is locked to the flipped position until the temporal noise amplitude is low enough so that the pump dominates the noise, flipping it back. In order to study this hypothesis, we use the fast polarimetry setup. The additional advantage with this setup is the ability to measure spin flips and other dynamic phenomena occurring in the range of nanoseconds to seconds.

## 4.2 Time and spin resolved measurements

The results in red bars presented in figure 4.3 regarding the PMT setup, show much improved degree of polarization at the higher temperatures compared to the previous experiment. Although they did not show any pin flipping for circular polarized excitation. The individual measurements are presented in figure 4.4.

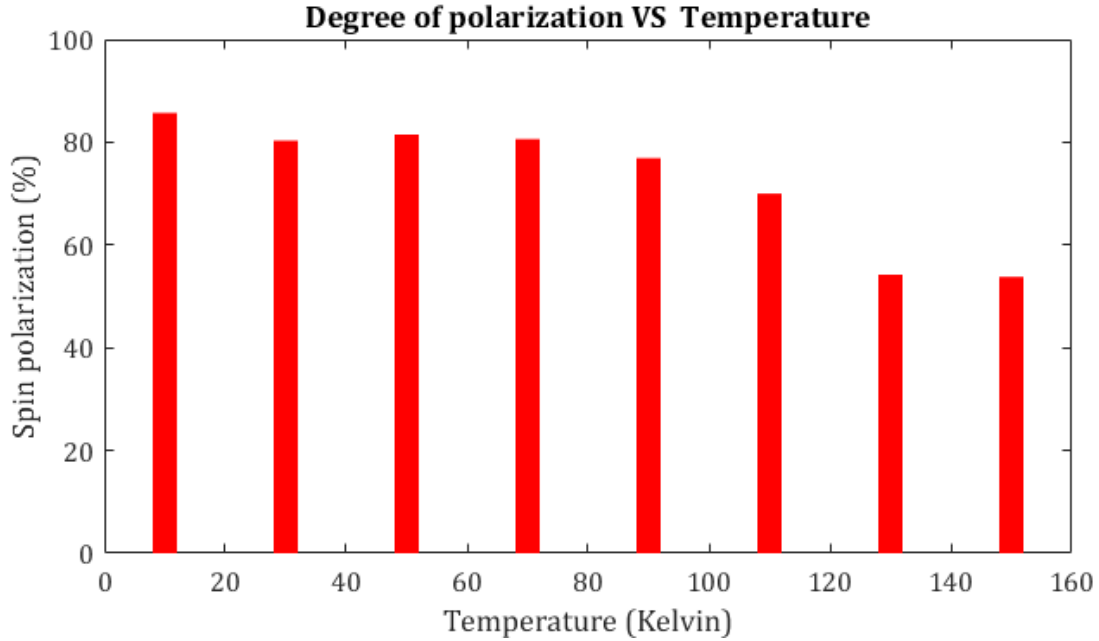


Figure 4.3. Extracted temperature dependence on the degree of polarization for  $\sigma^+$  excitation using relative intensities of a  $\sigma^+$  and a  $\sigma^-$  polarized beams detected by two PMT photosensors

The blue and red traces represent the intensity in arbitrary units of  $\sigma^-$  and  $\sigma^+$  polarized components of the polariton condensate. The green trace is the degree of polarization for every pair  $\sigma^+$  and  $\sigma^-$  data points. The y-axis is referring to the degree of polarization only, with the exception of the zero point that simultaneously represents zero intensity and zero degree of polarization.

As seen in the results in figure 4.4, there is no observable spin flip at higher temperatures. This first set of measurements seems to contradict the initial hypothesis that predicted that the origin of polarization loss is due to momentary spin flips as the spin noise floor rises with temperature. What we observe instead is that magnitude the trace with opposite polarization from the excitation rises above the background at elevated temperatures. Moreover, due to the higher lasing threshold, the available power of the excitation scheme does not seem to be sufficient to reach the optimal excitation power.

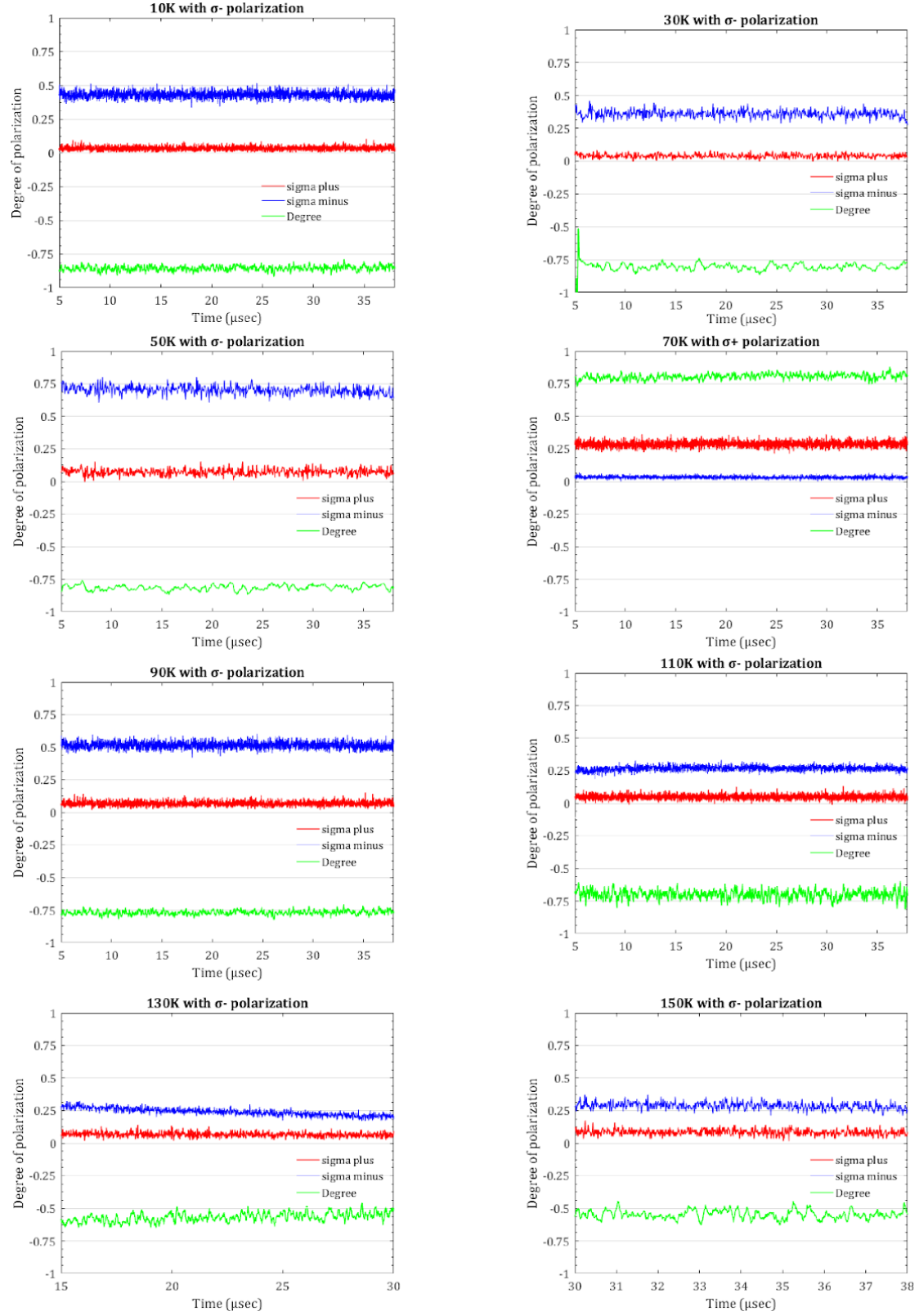


Figure 4.4. Polarization traces of polariton condensates excited by a circularly polarized beam

Due to the elevated power threshold for polariton lasing in higher temperatures, the CW laser source in conjunction with the DLP device are not able to provide sufficient power for observing polariton condensates above 150K. The maximum power of a gaussian laser beam is located near it's propagation axis while to generate a pattern that acts as a trap at the DMD, the center of the pattern is sent to the beam dump. The resulting power efficiency from the entire setup is around 15%.

#### 4.2.1 Spin flips

Spin flips are measured for a temperature range of 7K to 90K. The average spin flip rate is in part tuned with excitation power. It seems that except excitation power, the average flip rate is also dependent on the temperature, although there are not enough data points to make this observation statistically significant. With increasing temperature, the observed average flip rate increases. For cryogenic temperatures, it is possible to have polariton condensates stable for the entire realization which in our case is 100 $\mu$ secs (figure 4.5). This time window is determined by an intrinsic flickering of the DMD mirrors every 100 $\mu$ secs.

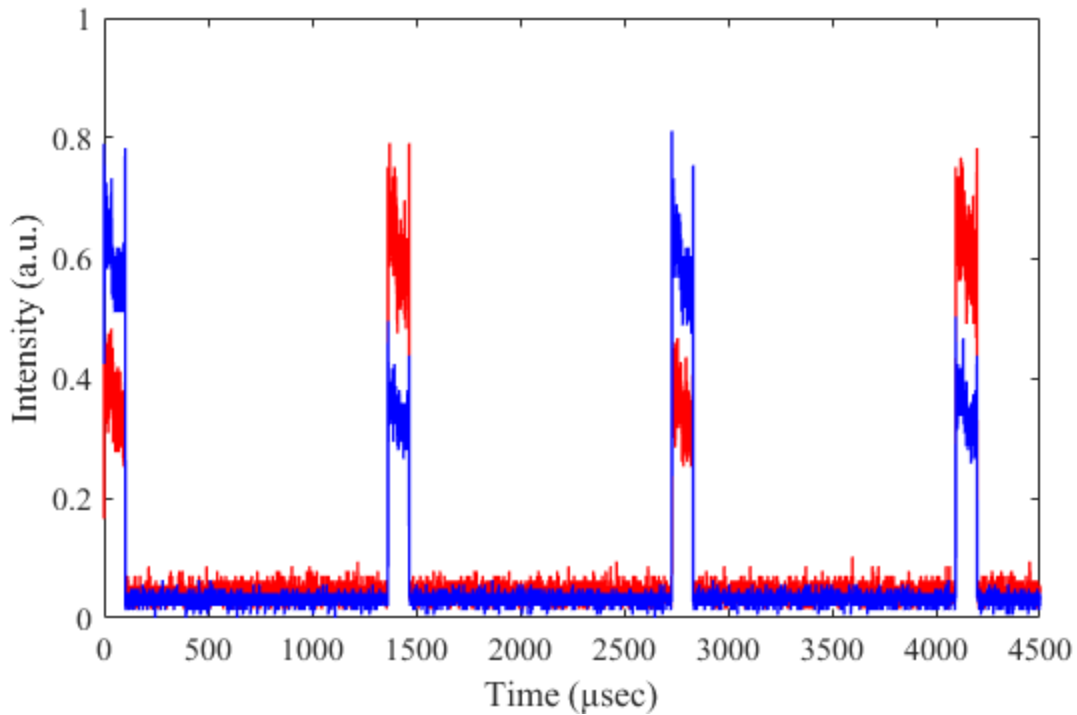


Figure 4.5. Wide time scale measurement with linear excitation. The polariton condensate randomly adopts either polarization state and remains stable for the whole realization at 30K.

Figure 4.6 shows spin flips within a single realization at 30K and 70K while figure 4.7 shows spin flips at 90K for two different excitation powers. For the same time period there are three spin flip for excitation power 1.8 times threshold while there are eighteen spin flips for excitation power just above threshold. To my knowledge, there are no other

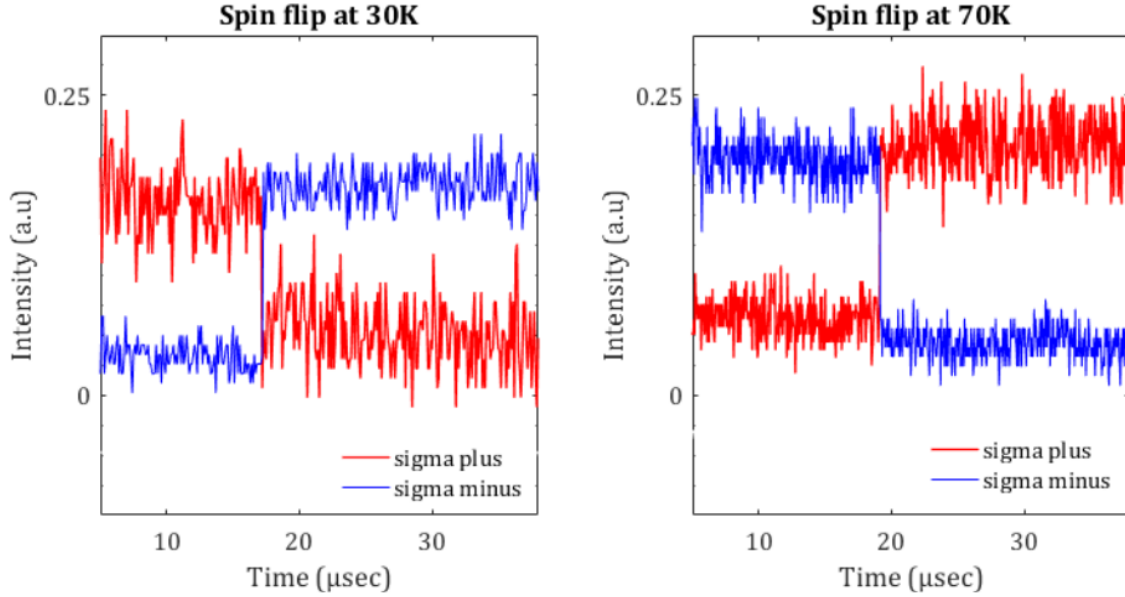


Figure 4.6. Spin flips at 30K and 70K

experiments showing spin flips for temperatures above 20K. In fact, [1] show that while observed spin state is stable for seconds at 5K, the flip rate increases exponentially above a certain temperature that they call  $T_c$ . According to their explanation, the thermal noise above  $T_c$  induces spin flips to the condensate within their measuring time window that was 1.5 msec with flip rates of about 35 spin flips per  $\mu\text{sec}$  at 18K. In our results, we have spin flip rate about of 1 spin flip per 10 $\mu\text{secs}$  at 90K. These observations could have a significant impact for applications in polariton condensate lattices. The ability to generate semi-stable stochastic flip states could be used for realizing systems optical spin based memories and random number generators. The degree of polarization for linear excitation seems to diminish compared to circularly polarized excitation although it still reaches a range of -40% to +40% at 90K. The minus sign represents the degree of polarization for  $\sigma^-$  polarized condensates while the plus sign represents the degree of polarization for  $\sigma^+$  polarized condensate. With the ability to control the spin state of polariton condensate, combined with the ability to create optical lattices with controlled barrier height, it is possible to create spin chains with controlled first neighbour interactions, with applications in complex optimization problems, neural networks etc.

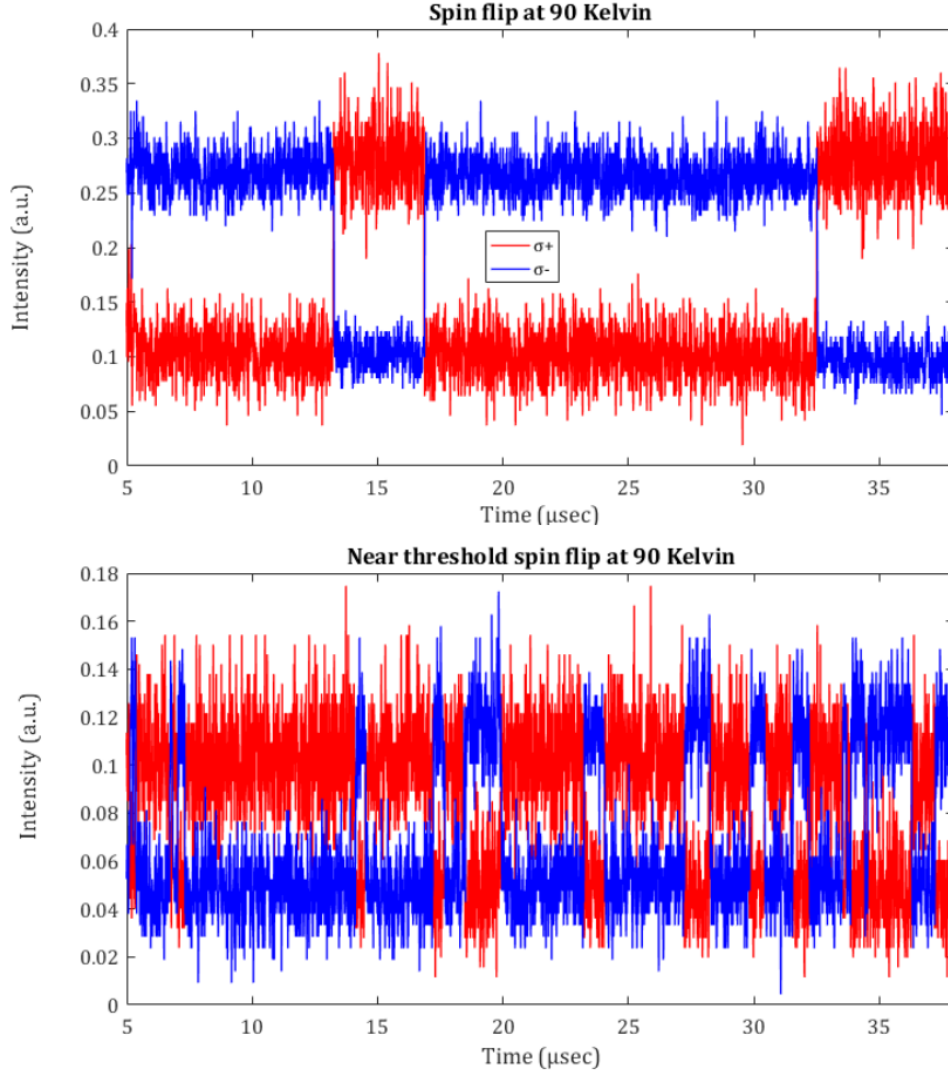


Figure 4.7. Spin flip at 90K. The upper figure is excited with

Here I present a simplistic qualitative conceptual model of the use of spinor polariton condensates with linearly polarized excitation for random number generators: Suppose the total spin noise of the system  $W$  with units of degree of polarization. Let us also suppose that the spin of the condensate flips when the degree of polarization noise is larger than 10% in the opposite spin. With these arbitrary parameters, we can simulate spin flips as shown in figure 4.8. The orange trace represents an ideal version of the polariton condensates degree of polarization ranging from -1 to 1 for  $\sigma^-$  and  $\sigma^+$  polarization respectively. Spin remains in its previous state for as long the degree of polarization of the spin noise does not exceed 10% for the opposite spin. The zero point represents random polarization and any value in between represent elliptical polarization. To generate an 8-bit random number using this behavior, we sample the degree of polarization of the condensate every  $(\text{Total\_relaxation\_time} / \#\_of\_bits) = 12.5$  time units

(green vertical lines). For this to work, the sampling frequency should be lower than the average fliprate. By arbitrarily treating -1 spin polarization as 0 and +1 as 1, we get an eight bit Random number. For the example of figure 4.8 it is *11100100* in binary which is 228 in decimal. Running this simulation 1000 times and extracting the random numbers yields the scatter plot and the histogram of presented in figure 4.9. Although that for this simulation I essentially used noise to generate noise, supposedly in the real world polariton example, this could be the way to harvest the ‘real’ randomness of the quantum world as opposed to the pseudo-random computer generated noise generated for this simulation.

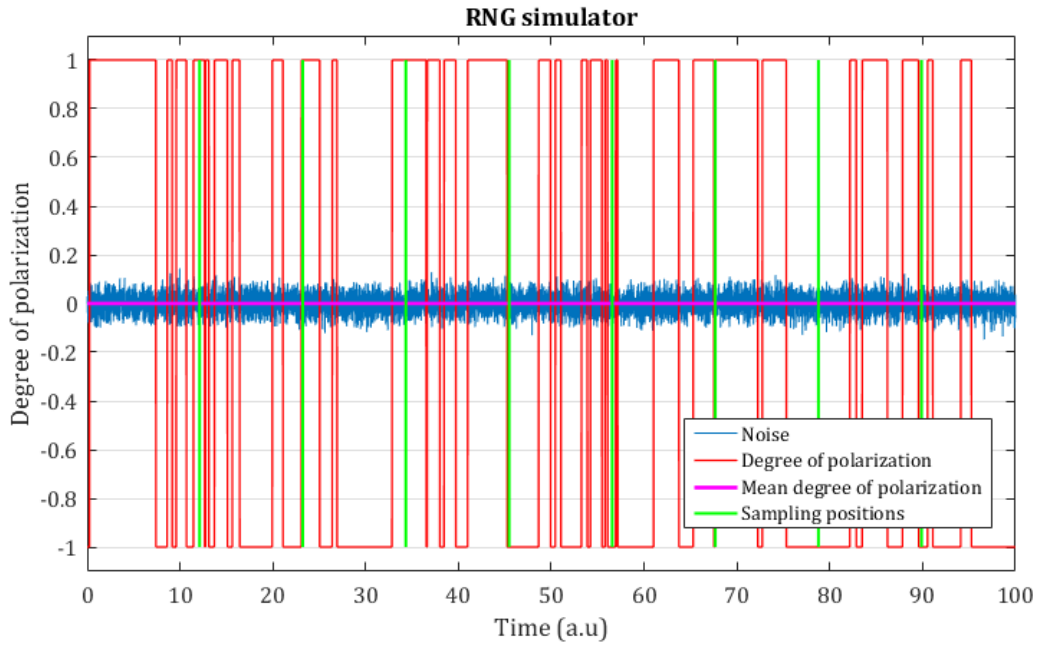


Figure 4.8. Simplistic simulation of spin flips and an example use for random number generators. The degree of polarization of polariton condensates (red) flips randomly between -1 and 1. The mean degree of polarization (magenta) for this timescale is close to zero meaning that the average duty cycle is close to 50%. Eight sample points taken at regular intervals (green) generate an 8-bit number.

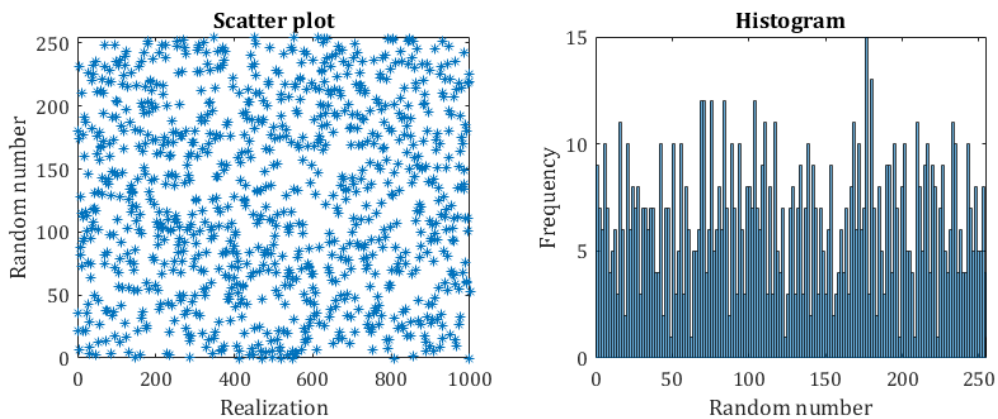


Figure 4.9. Scatter plot (left) and histogram (right) of 1000 8-bit numbers generated using the above simulation



## 5 Conclusions and perspectives

Microcavity polaritons show nine orders of magnitude lower effective mass than atomic systems. Since the critical temperature for condensation is inversely proportional to the effective mass, polaritons are suitable for studying condensed matter phenomena at a wide temperature range: from liquid helium to room temperature. Moreover, polariton condensates have macroscopic coherence lengths while they decay by emitting light from the microcavity containing all the information about the polaritonic state. This provides easy access and optical detection. Moreover, pumping the system using arbitrary patterns enables the creation of optical traps and polaritonic lattices with controlled first neighbour interactions. Polariton condensates exhibit pseudospin that corresponds to that of the exciton or the polarization of the coupled photon and is detectable by analysing the polarization state of emitted photons.

Studying the behaviour of interacting spin systems has implications ranging from combinatorial optimisation problems [49] to simulation of neural networks[50]. Since polaritons are able to form condensates at room temperature, this thesis aims to measure the temperature dependence of the spin polarization of trapped polariton condensates with real world applications in mind. We manage to observe spin polarization of over 85% at 10K and 54% for 150K for circularly polarized excitation. Moreover, for linearly polarized excitation, we measure record low spin flip rates at 90K .

While the above results are encouraging for the use of polariton condensates in real world applications, the mechanism for the loss of polarization high temperatures as well as the exact effect of temperature on spin flip rate is not yet fully understood. Such data can provide the seed for a more complete theoretical modeling for the effect of thermal noise on the spin polarization of trapped polariton condensates. Experiments with a pulsed laser could expand our available temperature range reaching room temperature. Finally, the realization of high temperature polariton condensates lattices with controlled nearest neighbour interaction could prove the viability of such systems for commercial applications.

## 6 References

1. I. Bloch and W. Zwerger, *Rev. Mod. Phys.* 80, 885 (2008).
2. A. Szameit and S. Nolte, *J. Phys. B* 43, 163001 (2010).
3. I. Carusotto and C. Ciuti, *Rev. Mod. Phys.* 85, 299 (2013).
4. T. Jacqmin, I. Carusotto, I. Sagnes, M. Abbarchi, D. D. Solnyshkov, G. Malpuech, E. Galopin, A. Lemaître, J. Bloch, and A. Amo, *Phys. Rev. Lett.* 112, 116402 (2014)
5. S. B. Nam, D. C. Reynolds, C. W. Litton, R. J. Almassy, T. C. Collins, and C. M. Wolfe, *Phys. Rev. B* 13, 761 (1976)
6. P. Y. Yu and M. Cardona, *Fundamentals of Semiconductors: Physics and Material Properties*. (Springer-Verlag, 1996).
7. S. A. Loureno; I. F. L. Dias; J. L. Duarte; E. Laureto; L. C. Poças; D. O. Toghinho Filho; J. R. Leite *Braz. J. Phys.* vol.34 no.2a (2004)
8. C. H. Henry and J. J. Hopfield, *Phys. Rev. Lett.* 15, 964 (1965)
9. M. Shinada and S. Sugano, *J. Phys. Soc. Japan*, 21:1936–1946, (1966)
10. R. L. Greene, K. K. Bajaj, and D. E. Phelps, *Phys. Rev. B*, 29:1807–188, (1984)
11. D. Chemla et al, *IEEE Journal of Quantum Electronics*, 20:265–275, (1984).
12. M. I. Dyakonov. *Spin Physics in Semiconductors*. Springer Series in Solid-State Sciences, vol 157. Springer, Berlin, Heidelberg, (2008).
13. A. Kavokin, J. J. Baumberg, G. Malpuech, and F. P. Laussy, *Microcavities*. (Oxford University Press, Oxford, 2007).
14. S. Pau, G. Björk, J. Jacobson, H. Cao, and Y. Yamamoto, *Phys. Rev. B* 51 14437-14447 (1995).
15. S. Rudin, T. L. Reinecke, and B. Segall, *Phys. Rev. B* 42, 11218 (1990)
16. H.-J. Miesner, D. M. Stamper-Kurn, M. R. Andrews, D. S. Durfee, S. Inouye, and W. Ketterle, *Science*, 279(5353):1005–1007, (1998)
17. A. Einstein. *Sitzungsberichte. Preussische Akademie der Wissenschaften*, 1(3) (1925)
18. S. N. Bose. *Z. Phys.*, 26:178–181 (1924)
19. P. G. Savvidis et al., *Phys. Rev. Lett.*, 84(7):1547–1550, (2000)
20. “Superfluid Helium 3”, by N.D. Mermin and D.M. Lee, *Scientific American*, (1976)
21. Grimm, R.. *Nature*. 435 (7045): 1035–1036. (2005)
22. Hau, Lene, *Society for Industrial and Applied Mathematics* (2006)
23. Giovanni Lerario et al., *Nature Physics* volume 13, pages 837–841 (2017)
24. A. Amo et al., *Nature*, 457(7227):291–295, (2009)
25. A. Imamoglu, R. J. Ram, S. Pau, and Y. Yamamoto, *Phys. Rev. A* 53, 4250 (1996)

26. E. Wertz et al. Nat. Phys., 6:860–864, (2010)
27. T. Gao et al. Phys. Rev. B., 85:235102– 1–235102–5, (2012).
28. A. Cristofolini et al. Phys. Rev. Lett., 110:186403–1–186403–5, (2013)
29. A. Askitopoulos et al. Phys. Rev. B 88, 041308(R) (2013)
30. H. Ohadi et al. Phys Rev X 5, 031002 (2015)
31. M. Z. Maialle, E. A. Andrada e Silva, L. J. Sham. Phys. Rev. B, 47(23):15776–15788, (1993)
32. I. A. Shelykh et al. Semicond. Sci. Technol., 25:013001 (47pp), (2010)
33. K. V. Kavokin et al., Phys. Rev. Lett, 92(1):017401–017404, (1993).
34. J. D. Jackson, Classical Electrodynamics, 2nd Edn. (Wiley, New York, 1975)
35. A. Askitopoulos et al., Phys Rev B 93, 205307 (2016)
36. B. Richards and E. Wolf, Royal Society (1997)
37. Wolf, S.A. et al., Science 294, 1488–1495 (2001)
38. Amo, A. et al. Nature Photon. 4, 361–366 (2010)
39. Paräiso, T.K., Wouters, M., Léger, Y., Morier-Genoud, F. & Deveaud-Plédran, B. Nature Mater. 9, 655–660 (2010).
40. Armitage, A. et al., Phys. Rev. B 55, 16395–16403 (1997).
41. Sturm, C. et al. Phys. Rev. B 91, 155130 (2015).
42. Alexander Dreismann et al., Nature Materials Letters (2016)
43. H. Ohadi et al., Phys. Rev. Letters 116, 106403 (2016)
44. H. Ohadi et al., Phys. Rev. Letters 119, 067401 (2017)
45. Yago del Valle-Inclan Redondo et al 2018 New J. Phys. 20 075008 (2018)
46. Sciamanna Mand Shore Nat. Photon. 9, 151–62 (2015)
47. L. Pickup et al. Phys. Rev. Letters 120, 225301 (2018)
48. A. P. D. Love et al. Phys. Rev. Lett., 101(067404), (2008)
49. S. Kirkpatrick, C. D. Gelatt, and M. P. Vecchi, Science 220, 671 (1983)
50. Andrzej Opala et al., Phys. Rev. Applied 11, 064029 (2019)